A Nonhydrostatic Version of the Penn State–NCAR Mesoscale Model: Validation Tests and Simulation of an Atlantic Cyclone and Cold Front

JIMY DUDHIA*

The Pennsylvania State University, University Park, Pennsylvania

(Manuscript received 3 July 1991, in final form 23 September 1992)

ABSTRACT

A nonhydrostatic extension to the Pennsylvania State University–NCAR Mesoscale Model is presented. This new version employs reference pressure as the basis for a terrain-following vertical coordinate and the fully compressible system of equations. In combination with the existing initialization techniques and physics of the current hydrostatic model, this provides a model capable of real-data simulations on any scale, limited only by data resolution and quality and by computer resources.

The model uses pressure perturbation and temperature as prognostic variables as well as a B-grid staggering in contrast to most current nonhydrostatic models. The compressible equations are solved with a split-time-step approach where sound waves are treated semi-implicitly on the shorter step. Numerical techniques and finite differencing are described.

Two-dimensional tests of flow over a bell-shaped hill on a range of scales were carried out with the hydrostatic and nonhydrostatic models to contrast the two and to verify the dynamics of the new version.

Several three-dimensional real-data simulations show the potential use of grid-nesting applications whereby the model is initialized from a coarser hydrostatic or nonhydrostatic model output by interpolation to a smaller grid area of typically between two and four times finer resolution. This approach is illustrated by a simulation of a cold front within a developing midlatitude cyclone, and a comparison of the front to observations of similar features.

The cold-frontal boundary was sharply defined at low levels and consisted of narrow linear updraft cores. At 2–4-km altitude this structure gave way to a more diffuse boundary with apparent mixing. Mechanisms are presented to explain these features in terms of inertial and shearing instability. Convection embedded in the frontal band formed a prefrontal line at later stages.

Finally, sensitivity studies showed that the frontal band owed its narrowness to the concentrating effect of latent heating. The frontal ascending branch was supplied by a strong easterly ageostrophic flow in the warm sector.

1. Introduction

The hydrostatic mesoscale model presented by Anthes and Warner (1978) has been employed to investigate meteorological phenomena on a wide range of scales ranging from continental-scale cyclone development to local valley flows. At the same time improvements have been made in the representation of the planetary boundary layer (Zhang and Anthes 1982), the surface radiation budget (Benjamin and Carlson 1986), the addition of several more cumulus parameterization schemes (e.g., Zhang and Fritsch 1986; Frank and Cohen 1987; Grell 1993), and an explicit moisture scheme (Hsie et al. 1984) with ice-phase processes (Dudhia 1989) for resolved-scale condensation. Grid nesting was also added by Zhang et al. (1986) and four-dimensional data assimilation by Stauffer and Seaman (1990).

With improvements in computer power it is becoming possible to use finer meshes. Higher resolution reduces errors associated with finite differencing; thus, it is clear that the future mesoscale model should not be constrained by the hydrostatic assumption, which effectively limits the resolution to around 10 km except in weak flow, nonconvective situations.

There are currently few nonhydrostatic models designed for use with "real data," that is, with data derived from three-dimensional observed wind, temperature, and moisture soundings. For a model to be generally applicable to such data requires that it can incorporate not only realistic topography and a diurnal radiative cycle but also surface fluxes of heat, moisture, and momentum that depend on local land or sea characteristics and a representation of boundary-layer processes. A horizontal coordinate compatible with the curvature of the earth's surface is also desirable if the model is to be applicable to large areas.

Existing nonhydrostatic real-data models include

* Current affiliation: MMM Division, NCAR, Boulder, Colorado.

Corresponding author address: Dr. Jimy Dudhia, Visiting Scientist, NCAR/MMM Division, P.O. Box 3000, Boulder, CO 80307-3000.

one that has been developed by the United Kingdom Meteorological Office (see Tapp and White 1976; Carpenter 1979). This model is typically employed with a 10–15-km grid over an area of 60 × 60 grid lengths. The Colorado State University model of Tripoli and Cotton (1982) has also been applied to regional simulations. Another such model presently under development is that of Tanguay et al. (1990), which incorporates semi-Lagrangian advection.

In addition to increasing the resolution beyond that of present hydrostatic model simulations, a nonhydrostatic model can be used for much more localized studies by resolving topographical, urban, and coastal effects, and deep convection through modeling their interactions with larger-scale weather systems on a nested grid model. Thus, the range of simulation capability would be substantially increased.

A new nonhydrostatic model is introduced in this paper. A primary consideration in its development is compatibility and strong overlap with the existing hydrostatic Pennsylvania State University–National Center for Atmospheric Research (Penn State–NCAR) Mesoscale Model to the extent that routines such as those handling advection, diffusion, radiation, the boundary layer, surface slab model, cumulus parameterization, and moisture can be incorporated into the new model with few modifications. In this way future improvements in these routines for the hydrostatic model can be equally applied to the nonhydrostatic model and vice versa.

The model has been used in a study of an Atlantic cold front providing a unique view of mesoscale structures that might exist in such systems. While warm-season and tropical convective systems such as squall lines have been simulated often, the three-dimensional small-scale aspects of cold-frontal structure have rarely been simulated until now. This may be due to the complexity of initializing an idealized yet realistic front in a model due to the need, in order to avoid spurious waves, for a well-balanced thermal- and gradient-wind flow with strong ageostrophic circulations, a background baroclinic circulation, and adequate boundary conditions that are consistent with the interior. For the nonhydrostatic model, initializing with real data and nesting gives the desired balances between the frontal and larger scales.

Conceptual models of cyclone cold fronts developed from analysis of synoptic data have more recently been enhanced by radar and aircraft studies to give some consensus on features that may accompany these systems, but it is only now that both models and computers have become capable of resolving them. Examples that will be detailed later in this modeling study are the warm conveyor belt, the prefrontal rainband, the narrow cold-frontal rainband, and the convective postfrontal boundary layer.

In section 2 the nonhydrostatic model equations will be presented, and the modifications to the Penn State–NCAR hydrostatic model will be discussed. Section 3 and the Appendix will describe the numerical methods employed in the model. Two-dimensional tests on a range of scales in an idealized flow situation will be presented in section 4, while section 5 shows three-dimensional results for a real case of a midlatitude cyclone and its cold front that have been simulated at several grid resolutions. A description of the dynamical processes in the cold front is also included to demonstrate the potential value of such a model in aiding the understanding of real weather systems.

2. Model equations

a. The equation set

The model is based upon a set of equations for a fully compressible atmosphere in a rotating frame of reference. Additional features include terrain-following coordinates and a map scale factor very similar to those of the hydrostatic model (Anthes and Warner 1978).

When the hydrostatic approximation is made, the vertical integration of the horizontal convergence serves to define both the surface pressure tendency and the vertical motion in a grid column. For the nonhydrostatic equations, however, separate predictive equations are required for the three-dimensional pressure distribution and the vertical momentum. The pressure tendency equation can be derived from the perfect gas law and mass continuity equations. The pressure perturbation in the model, p', is the predicted variable rather than full pressure. The model variables are thus pressure perturbation p', the three momentum components (u, v, w), the temperature T, specific humidity, and optionally cloud- and rainwater variables.

In the nonhydrostatic model it is also possible to retain the full three-dimensional Coriolis torque, not just the vertical component traditionally used in hydrostatic models. In practice though, it has been found, at least for cyclone-scale simulations, that the other components are negligible; thus, they will be omitted from the following equations.

b. Vertical coordinate

The hydrostatic model has a σ pressure coordinate in which the model levels are at constant σ where $\sigma = (p - p_{\text{top}})/p^*$ and $p^* = p_{\text{sfc}} - p_{\text{top}}$. The top pressure is constant so the upper boundary of the hydrostatic model represents a free surface while p^* is predicted. Thus, the pressure at a given model level is found from $p = p^*\sigma + p_{\text{top}}$, and this varies with time as the surface pressure varies.

It is possible to use the same coordinate in a nonhydrostatic model, as demonstrated by Miller and White (1984). However, in their equation set the surface pressure is still obtained with a hydrostatic tendency equation for p^*, so the coordinate is not fully based upon nonhydrostatic pressure. Their equations

result in a three-dimensional diagnostic equation for geopotential height similar to that for pressure in anelastic models.

Laprise (1992) introduces an equation set in which just the hydrostatic part of the pressure is used as a basis for a terrain-following σ coordinate while the full nonhydrostatic pressure is calculated from a prognostic relation. However, height-based coordinate systems are more commonly used in nonhydrostatic models.

Another option is to use the *reference-state* pressure p_0 to define a σ coordinate. In such a system p^* is constant with time and depends only upon the terrain altitude, while the σ levels are also fixed in space, so the coordinate is more closely related to height than pressure. A given grid point remains at a fixed height above the surface, and the top of the model domain is a surface of constant height. Therefore, the coordinate is exactly equivalent to a terrain-following height coordinate that is based on a suitably stretched function of z. The pressure at a point is given by $p = p^*\sigma + p_{\text{top}} + p' = p_0 + p'$ where p' is a predicted quantity. Implementation of this coordinate requires little change in the physics routines of the Penn State–NCAR Mesoscale Model, a major factor in choosing it for the new nonhydrostatic version.

The basic model equations can be written in this (x, y, σ) coordinate system as follows after subtracting large canceling terms from the vertical momentum equation:

$$\frac{\partial p'}{\partial t} - \rho_0 g w + \gamma p \nabla \cdot \mathbf{v} = -\mathbf{v}\cdot\nabla p' + \frac{\gamma p}{T}\left(\frac{\dot{Q}}{c_p} + \frac{T_0}{\theta_0} D_\theta\right), \quad (1)$$

$$\frac{\partial u}{\partial t} + \frac{1}{\rho}\left(\frac{\partial p'}{\partial x} - \frac{\sigma}{p^*}\frac{\partial p^*}{\partial x}\frac{\partial p'}{\partial \sigma}\right) = -\mathbf{v}\cdot\nabla u + fv + D_u, \quad (2)$$

$$\frac{\partial v}{\partial t} + \frac{1}{\rho}\left(\frac{\partial p'}{\partial y} - \frac{\sigma}{p^*}\frac{\partial p^*}{\partial y}\frac{\partial p'}{\partial \sigma}\right) = -\mathbf{v}\cdot\nabla v - fu + D_v, \quad (3)$$

$$\frac{\partial w}{\partial t} - \frac{\rho_0}{\rho}\frac{g}{p^*}\frac{\partial p'}{\partial \sigma} + \frac{g}{\gamma}\frac{p'}{p} = -\mathbf{v}\cdot\nabla w + g\frac{p_0}{p}\frac{T'}{T_0} - \frac{gR_d}{c_p}\frac{p'}{p} + D_w, \quad (4)$$

$$\frac{\partial T}{\partial t} = -\mathbf{v}\cdot\nabla T + \frac{1}{\rho c_p}\left(\frac{\partial p'}{\partial t} + \mathbf{v}\cdot\nabla p' - \rho_0 g w\right) + \frac{\dot{Q}}{c_p} + \frac{T_0}{\theta_0} D_\theta. \quad (5)$$

In the above, subscript 0 denotes reference state and primes denote deviations from the reference state. The density is ρ, the potential temperature is θ, the heating rate due to diabatic processes (i.e., latent heat and radiation) is $\dot{Q}$, and subgrid-scale eddy terms are represented by D_ϕ. The constants g, f, R_d, c_p, and γ represent acceleration due to gravity, Coriolis term, gas constant for dry air, heat capacity at constant pressure of air, and the ratio of heat capacity for air at constant pressure to that at constant volume.

The advection terms may be expanded for any variable A as

$$\mathbf{v}\cdot\nabla A \equiv u\frac{\partial A}{\partial x} + v\frac{\partial A}{\partial y} + \dot{\sigma}\frac{\partial A}{\partial \sigma}, \quad (6)$$

where the "coordinate velocity" used for advection, $\dot{\sigma}$, is related to the model-predicted velocity components by

$$\dot{\sigma} = -\frac{\rho_0 g}{p^*} w - \frac{\sigma}{p^*}\frac{\partial p^*}{\partial x} u - \frac{\sigma}{p^*}\frac{\partial p^*}{\partial y} v. \quad (7)$$

The upper and lower boundaries are taken to be rigid surfaces so $\dot{\sigma} = 0$ is applied as the boundary condition at $\sigma = 0$ and $\sigma = 1$. For (7) free-slip (i.e., zero-gradient) conditions are applied to obtain the horizontal velocity at these boundaries. The divergence term in (1) can be expanded in (x, y, σ) coordinates as

$$\nabla\cdot\mathbf{v} = \frac{\partial u}{\partial x} - \frac{\sigma}{p^*}\frac{\partial p^*}{\partial x}\frac{\partial u}{\partial \sigma} + \frac{\partial v}{\partial y} - \frac{\sigma}{p^*}\frac{\partial p^*}{\partial y}\frac{\partial v}{\partial \sigma} - \frac{\rho_0 g}{p^*}\frac{\partial w}{\partial \sigma}. \quad (8)$$

Over a flat surface p^* is constant, and the second and fourth terms on the right disappear.

c. *Moisture and heating*

The conservation equations for moisture with transfer terms between various categories such as vapor, cloud, and rain (q, q_c, and q_r, respectively, see Hsie et al. 1984) can easily be added to the above equations. Latent and radiative heating contribute to $\dot{Q}$. Virtual temperature perturbation $T'_v = T_v - T_0$ replaces T' in (4) and $\rho = p/R_d T_v$ in (2)–(5). A liquid drag term, $-g(q_c + q_r)$, may also be added to the buoyancy terms. The value of c_p can be modified for moist air but γ is assumed to remain constant irrespective of water vapor content and the reference state is taken to be dry.

It has been found (Klemp and Wilhelmson 1978) that the last two terms in parentheses in (1), representing the contribution of diabatic effects and subgrid-scale heat flux convergence to the pressure tendency, can be neglected, thereby saving several computations. However, a fact that has not been considered yet is that a model with a rigid upper boundary may behave more realistically without these terms in some situations. Specifically, their removal remedies the overheating caused by vertical confinement by allowing the model atmosphere to mimic free expansion. A particular case where the effect may be important is that domain-scale

clear-air radiative cooling would be somewhat overestimated without the modification. The role of the $\dot{Q}$ term in (1), which we choose to neglect, is to increase the pressure and thereby force expansion in regions of heating, generating acoustic and gravity waves. Dropping the term amounts to neglecting the small part of the velocity field that is directly due to expansion while allowing the temperature to change as if free expansion at constant pressure were occurring. It is also consistent with the assumption that the saturation adjustment is isobaric in the model's calculation of condensation and evaporation.

d. *Sound waves and gravity waves*

Equations (1)–(4) have been written in a form that isolates the acoustic (high-frequency) terms on the left of the equations following Klemp and Wilhelmson (1978). Such a division into high- and low-frequency terms has been shown to be extremely beneficial to model efficiency when a time-splitting scheme is used whereby high-frequency terms alone are evaluated on a shorter time step. The advantage is particularly marked when gravity wave speeds permitted by the model are much less than the speed of sound (300–350 m s^{-1}).

The use of a rigid upper boundary condition instead of a free-surface condition eliminates external gravity waves that may have speeds comparable with those of sound. It is these waves that restrict the time step in the hydrostatic version of the model, except when a "split-explicit" scheme is used for deep modes. Internal gravity waves provide a corresponding limit for models bounded by a rigid lid. However, for typical heights, lengths, and atmospheric static stabilities of the model's domain, these waves allow for a significantly longer time step than sound waves and so time splitting can be used.

Another constraint on the longer time step is the basic flow that Doppler shifts the gravity wave frequencies. Also, for grid lengths less than about 10 km and vertical grid lengths less than 1 km, the Courant number stability condition for vertical motion in strongly convective regions can provide a greater limitation to the time step than internal gravity waves. Allowing for these factors, the model equations can be stably integrated in time.

A feature of the equations that is unusual for nonhydrostatic models is that temperature, rather than potential temperature, is a predicted variable. This may have advantages in real-data assimilation where temperature is provided and in moisture and radiation calculations that require the temperature. However, there is an adiabatic warming term $(Dp/Dt)(\rho c_p)^{-1}$ in the temperature prediction equation (5), and representation of unresolved vertical turbulent mixing requires that potential temperature be calculated.

The use of temperature as a variable merits some consideration, as it is a distinctive aspect of this nonhydrostatic model. Note that the buoyancy term $g\rho'/\rho$ has been split into an acoustic term, $gp'/\gamma p$, and a nonacoustic sum of two terms, $-(gT'/T_0)(p_0/p) + (gR_d p'/c_p p)$, in (4). This contrasts with an earlier model of Cotton and Tripoli (1978), who did not treat the first term as acoustic. The last two terms correspond to $-g\theta'/\theta_0$; this is considered nonacoustic because sound waves do not substantially affect the potential temperature. Hence, this part of the buoyancy does not vary as sound waves propagate through a given point even though the pressure and temperature perturbations separately do undergo acoustic oscillations. Note that since these high-frequency temperature variations are assumed to have no feedback on the sound waves in the model equations, temperature does not need to be predicted on the shorter time step, but its variation on the long time step must remain consistent with that of pressure if acoustic oscillations in the two terms, $(gT'/T_0)(p_0/p) - (gR_d p'/c_p p)$, are to cancel each other.

From the above arguments it is important that the three pressure terms common to (1) and (5), that is, those in parentheses in (5), are treated consistently if the model is to handle the buoyancy correctly and approximately conserve potential temperature (entropy) in dry-adiabatic motion. Further details of the coupling between temperature and pressure are described in subsection 3d.

3. Numerical method

Much of the finite differencing remains as in Anthes and Warner (1978), particularly the advection terms (see subsection 3b), but the addition of two more predicted variables, p' and w, and removal of one, p^*, has necessitated changes and additions to their equations. These will be summarized in this section and are detailed in the Appendix.

a. *Grid structure*

As in the Penn State–NCAR hydrostatic model, the grid has a type-B staggering (Arakawa and Lamb 1977) of horizontal velocity variables with respect to the nonvelocity variables. This is illustrated in Fig. 1, which also shows that the vertical velocity is defined on the σ surfaces while the other variables are defined halfway between these levels.

Use of the B grid requires more averaging than the C grid in the finite-difference equations to obtain the horizontal velocity divergence, fluxes of variables and pressure gradients, and less averaging for the Coriolis terms. Haltiner and Williams (1980) have shown that the B-grid structure has numerical properties comparable with those of the C grid, especially if features are resolved by three or more grid lengths.

Nonhydrostatic modelers, with the exception of Miller and Pearce (1974) in an early version of their

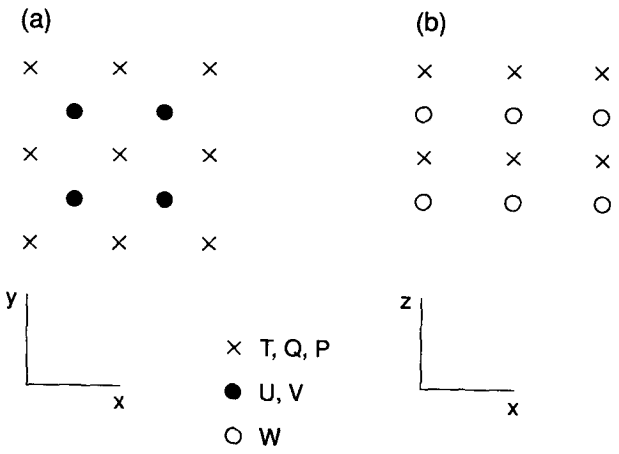

FIG. 1. The B-grid staggering of the variables (a) in x–y plane showing the staggering of horizontal velocity with respect to thermodynamic variables, and (b) in x–z plane showing the staggering of vertical velocity with respect to thermodynamic variables. Cross points; T, q, p'. Dot points; u, v. Circle points: w.

model, have generally used C-grid staggering. Therefore, the current model is an exception in this respect, but there is a definite gain in efficiency when the fully compressible equations are differenced on a B grid. If one carries out stability analyses for sinusoidal horizontally propagating sound waves on the three-dimensional B and C grids, using the relevant finite-difference scheme (described later), one finds that the B grid permits a maximum time step $\sqrt{2}$ times greater.

b. Advection

Anthes and Warner (1978) converted the advective terms in the finite-difference equations to flux form using the hydrostatic continuity relation. In this form finite differencing adds the advantage of conserving the advected quantity. With the nonhydrostatic model's equations, such a conversion is not exact and a residual term arises similar to that shown by Wilhelmson and Chen (1982). For a quantity A, the substantial derivative multiplied by p^* can be represented as

$$p^* \frac{DA}{Dt} \equiv \frac{\partial}{\partial t} p^* A + \frac{\partial}{\partial x} p^* u A + \frac{\partial}{\partial y} p^* v A + \frac{\partial}{\partial \sigma} p^* \dot{\sigma} A - A\left(\frac{\partial}{\partial x} p^* u + \frac{\partial}{\partial y} p^* v + \frac{\partial}{\partial \sigma} p^* \dot{\sigma}\right). \quad (9)$$

The hydrostatic model does not have the extra term in parentheses that is canceled by the surface pressure tendency. In the nonhydrostatic version, having p^* dependent only upon terrain, this additional term represents a local mass divergence, $(p^*/\rho_0)\nabla \cdot \rho_0 \mathbf{v}$. It is smaller than the flux term, given by the second to fourth terms on the right, but if there are significant density deviations from the reference state, the mass divergence term will be important.

The finite-difference form of the mass divergence is made the same as that of the surface pressure tendency in Anthes and Warner's hydrostatic model. It is consistent with the flux part such that when flux and mass divergence are added together, an advection-like finite-difference term results. Although the inclusion of this extra term disrupts the conservation properties of the model, it is more accurate than completely neglecting mass divergence in a fully compressible model.

Ikawa (1988) suggests that including the mass divergence term can help to keep the model numerically stable if sound-wave amplitudes grow large, but adequate filtering can control this growth without the term. The decreased sensitivity of the so-called advective form to sound waves is probably because in this form, in which the mass divergence is subtracted, sound-wave oscillations are canceled out while the flux form retains them.

The spatial finite differencing of the advection terms is the second-order centered scheme. However, there is an option for the first-order upstream scheme to be used for cloud and rain fields whereby the generation of negative perturbations is avoided.

c. Pressure gradient terms

The horizontal pressure gradient in (2) and (3) has two terms; the first is normally much larger. The primary term in (2) is differenced similarly to the corresponding terms of the hydrostatic model (see Appendix). The pressure gradient over terrain is generally better estimated by the nonhydrostatic model. There are problems with large terms of opposite sign in the hydrostatic model's pressure gradient. These problems can lead to spurious noise over steep terrain (Mesinger et al. 1988; Kuo et al. 1988) and are largely circumvented by using the local perturbation pressure terms in the momentum equations. For a reference state closer to the actual state the pressure gradient becomes more accurate.

d. Time-splitting scheme and acoustic waves

It was noted in subsection 2d that some terms in the nonhydrostatic version need a shorter time step because of their representation of sound-wave propagation, in particular the pressure terms and gradients in the momentum equations and the velocity divergence and reference-state advection in the pressure equation. The leapfrog scheme of the hydrostatic model is retained for the long time step with the Asselin filter; however, the Brown and Campana (1978) scheme is not used.

Time-splitting to represent sound waves has been employed in several meteorological numerical models, for example, Klemp and Wilhelmson (1978), Tripoli and Cotton (1982), and Ikawa (1988). The technique involves using a number of short time steps to span the time from $(n-1)\Delta t$ to $(n+1)\Delta t$, to predict the

velocity and pressure fields. Here Δt is the long time step and n increments by one for each long time step. The "slow" tendencies such as advection, Coriolis acceleration, and buoyancy acceleration are evaluated first at the long step n; diffusion, cloud microphysics, and vertical subgrid-scale flux convergence terms are evaluated at $n - 1$; and all are kept constant during the time integration from $n - 1$ to $n + 1$. Typically there may be four to seven short time steps to each $2\Delta t$ leapfrog step.

The procedure for advancing one short time step from time τ to $\tau + 1$ is as follows:

(i) Predict $u^{\tau+1}$ and $v^{\tau+1}$ from p'^{τ} with a forward time step;

(ii) Predict $w^{\tau+1}$ from a time average of $p'^{\tau+1}$ and p'^{τ};

(iii) Predict $p'^{\tau+1}$ from $u^{\tau+1}$, $v^{\tau+1}$, and a time average of $w^{\tau+1}$ and w^{τ}.

Steps (ii) and (iii) are combined as implicit time steps and entail solving a tridiagonal matrix for the vertical velocity in each grid column. This is done efficiently with a direct recursive method. The time averaging can be done as follows:

$$\bar{w}^{\beta} = \frac{1}{2}(1 + \beta)w^{\tau+1} + \frac{1}{2}(1 - \beta)w^{\tau}.$$

The implicit equation is of a Crank–Nicholson type. If β is set to zero, the time-centered averaging of Klemp and Wilhelmson results. This scheme is neutral with respect to sound-wave growth. For β equal to one, the scheme follows one shown by Ikawa (1988) to be neutral to horizontally propagating sound waves while strongly damping the vertically propagating ones.

The implicit treatment of vertically propagating sound waves allows a time step independent of the vertical resolution and is therefore important to the efficiency of a model where this resolution is typically much better than the horizontal resolution. In such a scheme, however, vertically propagating sound waves are generally retarded. Since propagating acoustic waves reflect off the upper, lower, and lateral boundaries, trapping acoustic energy within the domain, some form of damping is required to control acoustic noise. In practice, small positive values of β (e.g., 0.2) may be used to control vertically propagating sound waves (Durran and Klemp 1983). Using such an inherently damping finite-difference scheme efficiently reduces problems related to reflections from the top of the domain.

Damping of the horizontally propagating sound waves is effectively achieved by adding a small term directly proportional to the divergence [second plus third term on the left of (1)] onto the pressure perturbation in the horizontal momentum equations (Skamarock and Klemp, personal communication). Note that the added term tends toward zero as sound-wave amplitudes become small.

The coupling between the temperature and pressure perturbation tendencies was referred to in subsection 2d. The three terms common to both (1) and (5) were given by

$$\frac{Dp}{Dt} = \frac{\partial p'}{\partial t} + \mathbf{v}\cdot\nabla p' - \rho_0 g w. \tag{10}$$

If the terms are treated consistently in (1) and (5), the potential temperature will be quasi-conserved. In particular, the advection of pressure perturbation should not be neglected in a model with temperature as a prognostic variable.

As long as the methods of controlling sound-wave noise described earlier are employed, the above scheme provides a stable and inexpensive method of integrating the compressible equations on a terrain-following stretched grid with the benefits of having temperature and pressure readily available for microphysical–radiative computations.

With high-terrain features situations were found in which deep wave modes were trapped by the rigid upper boundary. These can be suppressed, however, by using an upper zone of enhanced horizontal diffusion or implementing the Klemp and Durran (1983) radiative condition at the top of the model.

4. Two-dimensional tests of the model

Before applying the model to complex three-dimensional real-data simulations, it is worth testing it against known flow solutions in a simpler situation. It can also be compared with a two-dimensional version of the hydrostatic model to verify its behavior at larger scales where nonhydrostatic effects are small.

The most widely used tests for new models (e.g., Clark 1977; Ikawa 1988; Xue and Thorpe 1991) involve simulating steady, dry, unsheared flow over a hill in a constant-stability environment. The solution for the linear situation, where the hill is low, is given by Queney (1948). Essentially, the modes seen in the steady solution are those that are forced by the hill and that have an upstream phase speed equal to the imposed flow, that is, are stationary relative to the hill.

If the effects of density stratification due to the pressure decrease with height are neglected, a simple expression relates the horizontal and vertical wavelengths of these modes to the basic flow speed u; the stability (Brunt–Vaisälä frequency) N; and the Coriolis parameter f; that is,

$$u^2 = N^2\lambda^2 + f^2\lambda_x^2, \tag{11}$$

where λ is the total wavelength per radian and λ_x is its horizontal component, so that

$$\lambda = (\lambda_x^{-2} + \lambda_z^{-2})^{-1/2}.$$

Thus, λ is always less than or equal to λ_x. If the hydrostatic approximation is made, λ in (11) becomes

λ_z and the solutions are significantly altered for shorter horizontal wavelengths.

For typical values of u (10 m s^{-1}), N (10^{-2} s^{-1}), and f(10^{-4} s^{-1}), stationary modes are shown in Fig. 2 where λ is plotted against $\log\lambda_x$. It can be seen that there are short- and long-wave cutoffs to the wave solutions. For horizontal wavelengths, λ_x, less than approximately u/N, or greater than about u/f, (11) has no real solutions. Therefore, within this range would be waves forced by the mountain while outside only decay-like modes would be seen.

An isolated hill forces a spectrum of horizontal wavelengths, some with a stationary vertical mode. The bell-shaped function used was given by $h = h_0[1 + (x^2/a^2)]^{-1}$ where h_0 is the height and a is the half-width parameter. Five hills were chosen with half-widths varying from 0.1 to 1000 km to cover the range of flow responses indicated by (11) and Fig. 2. The spectral amplitude functions of these hills per unit $\log\lambda_x$ are shown in Fig. 3. On this log scale, the maximum forcing per unit interval occurs for $\lambda_x = a$ with negligible forcing at $a/10$ and about one-quarter of the maximum at $10a$.

To simulate these five cases, grid lengths were chosen to be $a/5$, the domain length was $20a$, and the simulated time was $21.6a/u$ (usually 1080 time steps) which was enough time for a steady solution to be reached. The domain top was at around 15.3 km (100 mb), and there were 40 levels equally spaced in reference pressure. The reference state temperature was equal to the initial constant-stability profile temperature. The hill height was 400 m, giving $Nh/u = 0.4$, which is sufficiently low to be compared with linear analytic solutions. The lateral boundary conditions were a simple radiative type and a ten-layer (approximately 6 km deep) high-diffusion upper sponge was used for those simulations in which the energy propagated up to the top boundary. There were no heat sources, friction, or explicit vertical mixing in the domain. The flow was initiated as an unsheared 10 m s^{-1} flow that is uniformly faster above the hill to preserve horizontal mass flux. The initial streamlines, therefore, follow constant

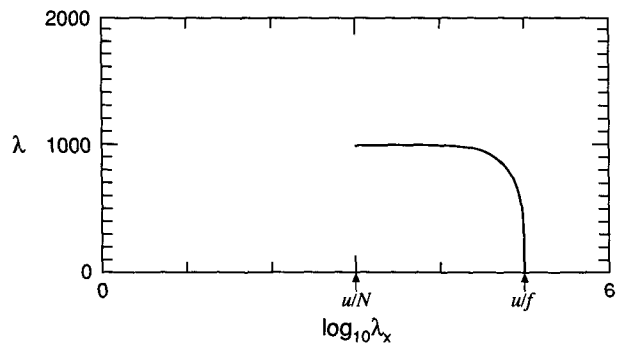

FIG. 2. Total wavelength λ (m) versus log of horizontal wavelength $\log_{10}\lambda_x$ for stationary wave modes.

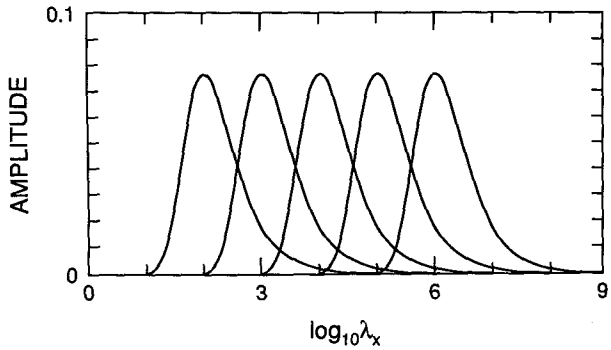

FIG. 3. Amplitude spectra versus log of horizontal wavelength, $\log_{10}\lambda_x$, for bell-shaped hills of five half-widths.

σ levels. The geostrophic wind was set at 10 m s^{-1} everywhere.

a. *Nonhydrostatic results*

Figures 4a–e display the vertical motion field at the end of the five simulations in the lowest 10 km of the domain. Their features are summarized below.

1) a = 100 m POTENTIAL FLOW

From Figs. 2 and 3, it can be seen that nearly all of the forcing due to the hill projects onto decay (or evanescent) modes. In this regime the flow passes over the hill on a time scale too short, compared to that of Brunt–Väisälä frequency oscillations, for steady gravity wave modes to be forced. No forced gravity waves are able to propagate upstream, so the flow is supercritical. The vertical scale of the motion (Fig. 4a) is similar to the half-width, a (=100 m), and so the influence of the hill is confined to low levels.

2) a = 1 km NONHYDROSTATIC GRAVITY WAVES

Here, the most strongly forced stationary wave modes have horizontal and vertical lengths of similar magnitude. The energy propagation, given by the overall tilt of the pattern (Fig. 4b), is distinctly downstream (rightward) from the hill. This is consistent with the nonhydrostatic waves' group speeds being less than their phase speeds. The phase tilt is consistent with the upward and leftward flow-relative energy propagation of these stationary modes.

3) a = 10 km HYDROSTATIC GRAVITY WAVES

In Fig. 4c the phase tilt is as in Fig. 4b but the overall pattern is upright, consistent with vertically propagating energy and the group speed being close to the phase speed. This is as expected for the hydrostatic regime where the vertical wavelength is only one-tenth of $2\pi a$, the most strongly forced horizontal wavelength. Note

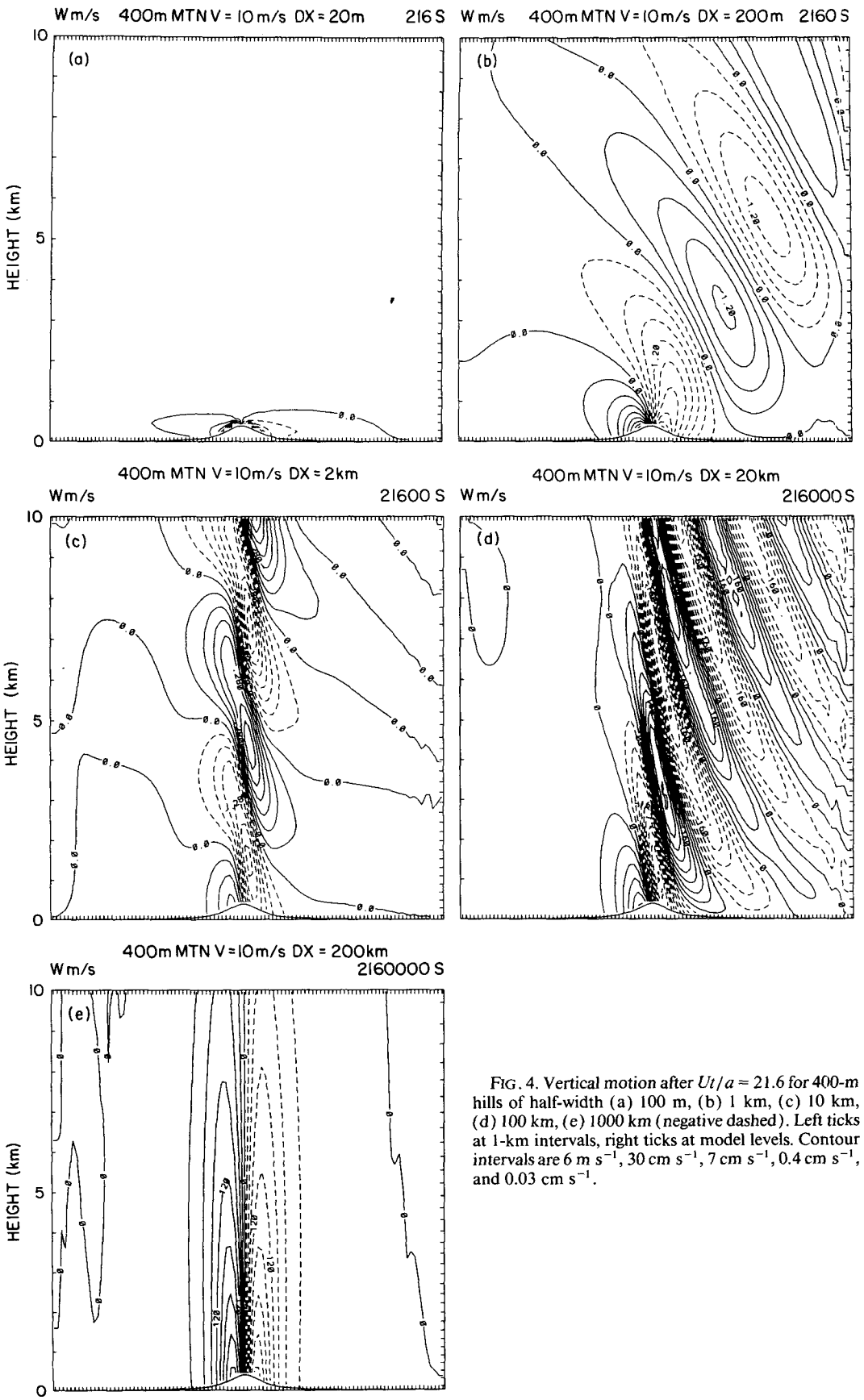

FIG. 4. Vertical motion after $Ut/a = 21.6$ for 400-m hills of half-width (a) 100 m, (b) 1 km, (c) 10 km, (d) 100 km, (e) 1000 km (negative dashed). Left ticks at 1-km intervals, right ticks at model levels. Contour intervals are 6 m s^{-1}, 30 cm s^{-1}, 7 cm s^{-1}, 0.4 cm s^{-1}, and 0.03 cm s^{-1}.

that an upper-level sponge was used in this and the next simulation to reduce reflection of energy from the upper model boundary.

4) a = 100 km INERTIAL GRAVITY WAVES

While the Coriolis force existed in the previous simulations, the time scale of the flow passing over the hill (a/u) was too short compared to $1/f$ for inertial effects to be noticeable. In Fig. 4d, however, downstream lee waves are present as the ageostrophic horizontal wind forced by the hill is acted upon by the Coriolis force. This continuously rotates the ageostrophic component about a vertical axis leading to regions of divergence and convergence and hence vertical motion downstream of the hill.

5) a = 1000 km QUASIGEOSTROPHIC FLOW

The inertia–gravity waves forced by this scale of hill propagate too rapidly for stationary modes to exist. By the end of the simulation (Fig. 4e) they have left the domain leaving a balanced flow with a normal velocity (not shown) up to about 3 m s^{-1} into the plane upstream of the hill and out downstream. This represents an anticyclonic turning of the flow as it traverses the hill. In quasigeostrophic terms, potential vorticity conservation requires that there be negative relative vorticity above the hill with zero upstream and downstream. The final exponential structure in the vertical velocity seen in Fig. 4e has a vertical scale given approximately by af/N = 10 km (Queney 1948).

b. Hydrostatic results

Identical simulations to those above were performed with the hydrostatic model. The results from this model, corresponding to those in Figs. 4c–e, were as expected, fairly indistinguishable from those of the nonhydrostatic model. For a = 10 km, Na/u = 10 while nonhydrostatic effects would only be expected to be significant for this factor being of order unity. This serves as an independent verification of the nonhydrostatic model's dynamics.

Differences are seen for a = 0.1 and 1 km. The hydrostatic model produces results almost identical to Fig. 4c for both cases. In fact, without the Coriolis force, the hydrostatic model, being insensitive to the horizontal scale, would produce identical patterns for all hill widths. Only the magnitude of the vertical velocity would vary in proportion to $1/a$.

c. Other tests

It is useful to check the model quantitatively against theoretical results. From Fig. 4c it can be seen that the vertical wavelength of the hydrostatic wave pattern is close to the predicted 6.28 km ($=2\pi u/N$).

In order to determine whether the nonhydrostatic lee waves such as those in Fig. 4b have the correct tilt, a simulation was run with a 1-km-high mountain. Here Nh/u = 1 so the case is quite nonlinear and, in fact, given sufficient time, wave breaking occurs because Nh/u exceeds the critical value of 0.85 found by Miles and Huppert (1969) for Boussinesq flows.

After only 1 h of simulation, the streamlines, represented here by isentropes (Fig. 5), are approximately vertical at about the 4-km altitude and downstream of the hill. At this stage it is possible to compare the position of maximum steepening with that found by Laprise and Peltier (1989). From their Fig. 9b it can be seen that with Na/u = 1 the maximum steepening should occur at approximately $0.47\lambda_G$ downstream of the hill crest, where $\lambda_G = 2\pi u/N$. That corresponds to about 2.9 km in this case and Fig. 5 shows that the model indeed produces its maximum steepening at this location. For a hydrostatic model the region would be displaced only 0.33 km from the crest.

5. Three-dimensional real-data simulations

a. Initialization

The primary goal of this work has been to apply a nonhydrostatic model to observed cases by making use of the existing analysis packages developed for the hydrostatic model. These analysis routines can take raw upper-air and surface data with gridded output from a global or limited-area data assimilation system or

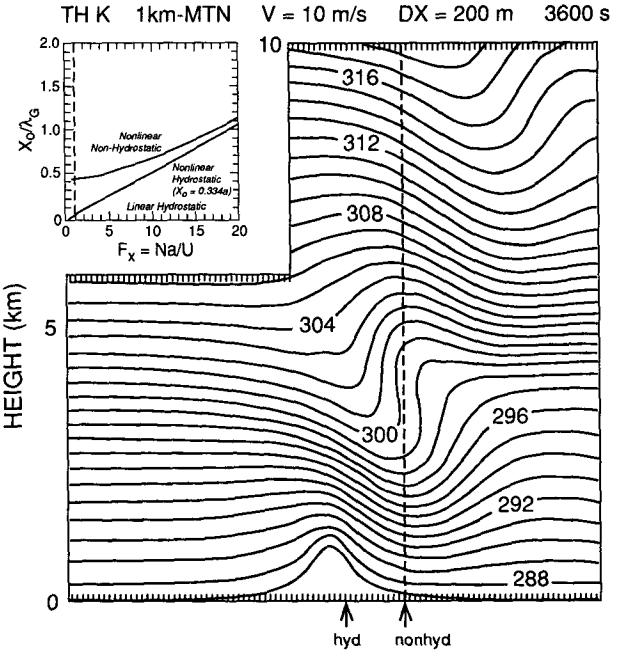

FIG. 5. The 1-km hill, half-width 1 km, potential temperature showing position of maximum steepening (dashed line) after 1 h. Contour interval 1 K. Inset shows dimensionless displacement versus Na/U (Laprise and Peltier 1989).

numerical weather prediction model to form a reanalysis on the model grid. Input data at later times are also reanalyzed on the model grid to provide lateral boundary conditions.

At present, the output of these initialization routines includes wind, temperature, and moisture data on the σ levels of the hydrostatic model together with surface pressure. These must be adjusted vertically to the nonhydrostatic σ levels, which are defined by reference pressure rather than actual pressure. In addition, two more three-dimensional fields must be initialized: the vertical momentum and pressure perturbation.

The reference profile of temperature as a function of pressure $T_0(p_0)$ chosen for this study was given by

$$T_0 = T_{s0} + A \ln\left(\frac{p_0}{p_{00}}\right), \tag{12}$$

where $T_{s0} = 280$ K, $A = 50$ K, $p_{00} = 1000$ mb.

The vertical velocity is obtained from vertical interpolation of pressure velocity (omega) that is estimated from continuity in the hydrostatic wind field. The nonhydrostatic model will not immediately have a mass flux balance because the velocity fields may produce some mass divergence, but the adjustment process is, in practice, quickly achieved by sound waves.

The pressure perturbation is calculated by vertical integration of the discretized form of the vertical momentum equation [see Appendix, Eq. (A7)] with the w terms set to zero. The lowest-layer value of p' is estimated from the surface pressure that is provided in the hydrostatic input data.

Input data files for later times are also interpolated vertically in order to provide lateral boundary conditions for the nonhydrostatic model. The boundary condition is a relaxation type in which the four points nearest the boundaries are relaxed toward specified values that are interpolated in time between the analysis times. This condition is applied to wind, temperature, water vapor, and pressure perturbation. Vertical momentum has a zero-gradient condition and liquid water is zero on inflow and zero-gradient on outflow.

There is also currently a capability of interpolating the nonhydrostatic model output to finer meshes so that more detailed simulations can be carried out over selected areas. In these, a one-way nesting technique is applied whereby data from the coarse mesh at, for instance, 1-h intervals provides the lateral boundary conditions to the fine mesh. The inclusion of finer-scale topographic features requires additional vertical adjustments in the model fields, but in simulations reported here only horizontally interpolated topography is used on the finer meshes.

b. *Real-data simulations*

In this section an account will be given of some simulations carried out on a North Atlantic explosive cyclogenesis case. These simulations illustrate the potential usefulness of the new model.

The oceanic cyclogenesis case chosen has been studied extensively by Kuo et al. (1991a,b) and occurred on 13–14 February 1982. The central pressure decreased by 44 mb to 954 mb in 24 h from 1200 UTC 13 to 1200 UTC 14 February as the storm propagated northeastward. Eventually it passed the southeast tip of Newfoundland and started to fill in. Further details of the synoptic situation can be found in Kuo et al. (1991b).

The data for the 20-km grid domain was interpolated from the results of a 40-km hydrostatic model run [which itself was initialized with data from an 80-km run that had been combined with observations in a reanalysis by Kuo et al. (1991a)]. Their hydrostatic simulation with a 20-km grid and 15 vertical levels reproduced the sea level pressure field very successfully, and cloud patterns compared well with satellite pictures of the system.

The nonhydrostatic model was run with the same physics including the high-resolution planetary boundary layer scheme (Zhang and Anthes 1982), surface heat, moisture, and momentum fluxes. However, for the case here, there were resolved cloud and rain processes (Hsie et al. 1984) instead of the nonconvective precipitation scheme, and the convective scheme was a simpler single-cloud version (Grell 1993) than the modified Arakawa and Schubert (1974) scheme used in the hydrostatic model. The model has also been run with the same physics as the hydrostatic model, and this showed that no significant changes in the cyclone track and deepening resulted from the above modifications. Convective rain contributed only 1%–2% of the total, and in fact results were almost identical in a test without a convective scheme. This finding was consistent with that of Kuo and Low-Nam (1990) for simulated explosive cyclones.

Here results from two nonhydrostatic simulations will be shown. The first is a 24-h simulation, starting at 2100 UTC 13 February 1982, with the same 20-km grid as the hydrostatic simulation referred to above. The domain had 91×121 horizontal grid points with 15 vertical levels at $\sigma = 0.05$, 0.15, 0.25, 0.35, 0.45, 0.55, 0.65, 0.74, 0.81, 0.865, 0.91, 0.945, 0.97, 0.985, and 0.995. It used 1-h boundary conditions derived from the 40-km hydrostatic simulation. Then a 6.67-km grid was interpolated from the 20-km model output and an 8-h simulation starting at 0500 UTC 14 February was run on 101×121 points centered on the cold front, with 1-h boundary conditions. A third simulation with a 10-km grid centered on the occlusion region will also be referred to briefly.

The long and short time steps were, respectively, 100 and 50 s for the 20-km simulation and proportionately reduced for the 6.67-km simulation. In comparison, the 20-km hydrostatic model used a 30-s time step and required approximately one-third more CPU

time for a 24-h simulation on the Cray Y-MP than the nonhydrostatic simulation.

1) CYCLONE SIMULATION (20-km GRID)

At the beginning of the simulation the central pressure at sea level was 979 mb. The time sequence in Fig. 6a and 6b shows the sea level pressure at 12 and 24 simulated hours. The central pressures at 6-h intervals are, respectively, 969, 961, 954, and 956 mb. The lowest pressure of 953 mb occurred at about 19 hours.

The development of the sea level pressure field of this cyclone can be compared with the hydrostatic model and observations presented by Kuo et al. (1991a). Figure 6c shows the nonhydrostatic (solid) and hydrostatic (dashed) models' sea level pressure fields at 15 h. There is a very close agreement despite model differences in numerics, physics, and dynamics. This is consistent with the fact that on the resolved scale, nonhydrostatic effects are not expected to be noticeable.

A simulation with a 10-km grid covering the cyclone low pressure center revealed the same central pressures as in the 20-km grid showing that the 20-km grid resolution of this feature was sufficient in this case.

Some features of this modeled cyclone are frequently observed. For instance, at 12 h the cold front is much more clearly visible in the water vapor field (Fig. 7a) than in the temperature field (Fig. 7b) at about 1-km altitude (σ = 0.865). The front is marked by a thin dry band and a discontinuity in the horizontal temperature gradient. The occluded front is clearly defined by both temperature and moisture fields northwest of the cold front and low pressure center (marked L). By this time the cold front is moving ahead of the surface low pressure center, which coincides with a warm moist pool that is almost cut off from the warm sector.

The vertical motion (Fig. 7c) at σ = 0.865 (near 875 mb) shows elongated mesoscale updrafts along the cold front, some ascent south of Newfoundland associated with the warm front, and weak curved banded structures approximately paralleling the isobars around the north of the cyclone. There is little vertical motion in the warm core where the lowest kilometer has a high static stability. At 12 h some of the cold-frontal updrafts extend to high levels having a maximum up to 2 m s^{-1} at around 500 mb and propagate rapidly northeastward with the upper-level frontal jet.

At 18 h the low pressure center and warm seclusion are separated from the cold front by 600 km. By this

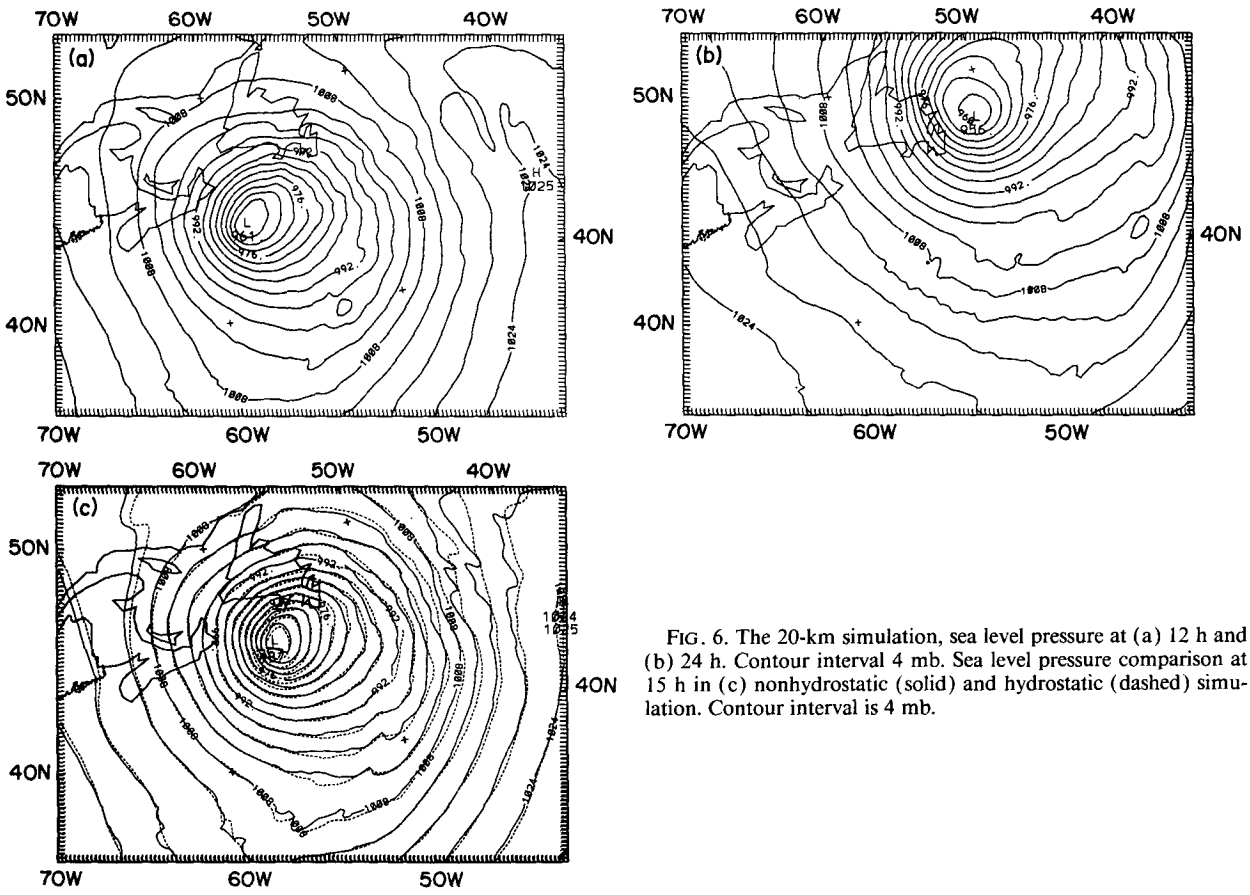

FIG. 6. The 20-km simulation, sea level pressure at (a) 12 h and (b) 24 h. Contour interval 4 mb. Sea level pressure comparison at 15 h in (c) nonhydrostatic (solid) and hydrostatic (dashed) simulation. Contour interval is 4 mb.

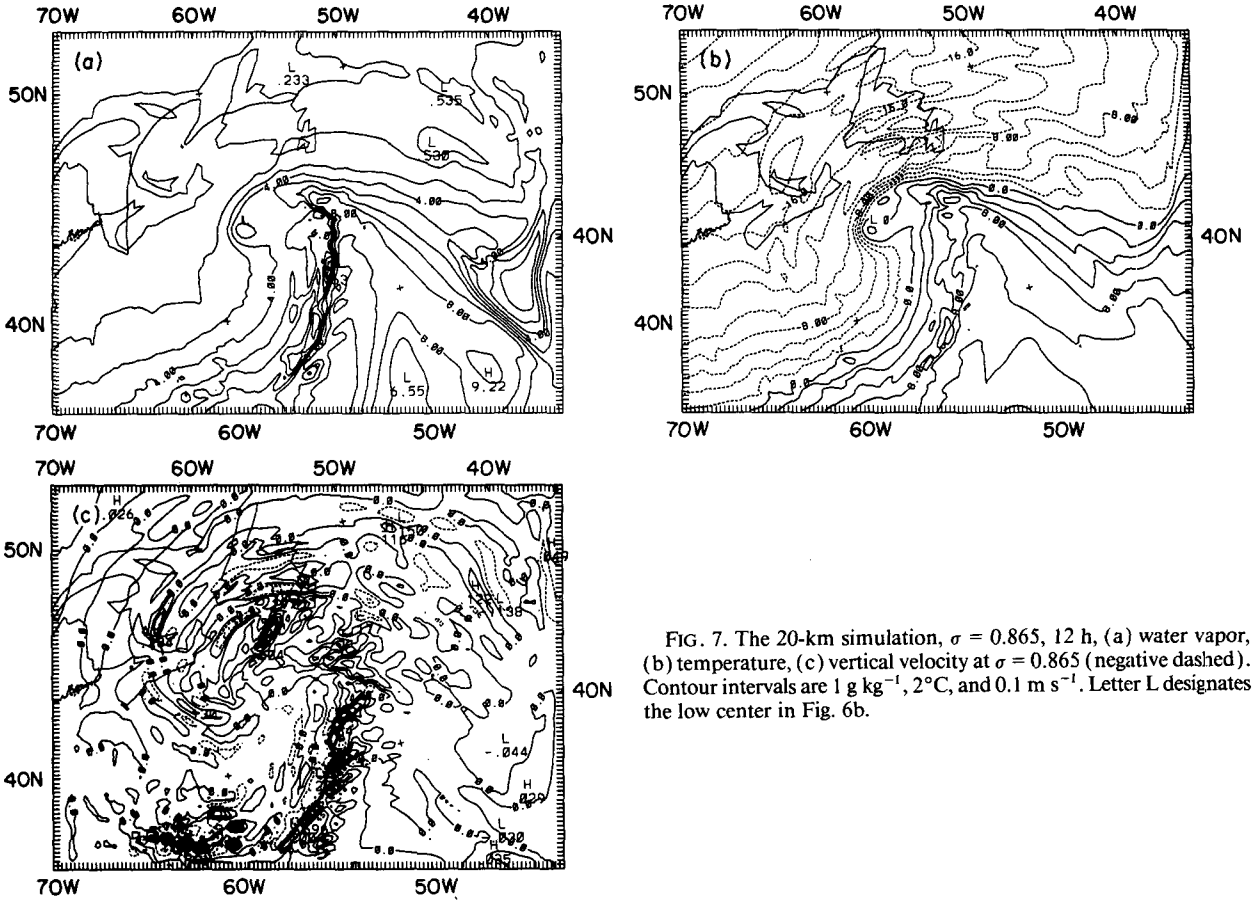

FIG. 7. The 20-km simulation, $\sigma = 0.865$, 12 h, (a) water vapor, (b) temperature, (c) vertical velocity at $\sigma = 0.865$ (negative dashed). Contour intervals are 1 g kg^{-1}, 2°C, and 0.1 m s^{-1}. Letter L designates the low center in Fig. 6b.

time the cold air to the rear of the front starts to become convective as it is advected over the warmer Gulf Stream water. The 10°C air–sea difference drives shallow weakly precipitating convection with tops up to 2 km, but this is coarsely resolved with the 20- and 10-km grids. Cloud and moisture structures (not shown) appear typical for midlatitude cyclones. There is a distinct comma cloud at 18 h with resolved updraft cores associated with the cold front at the southern tip. The dry tongue at upper levels wraps around the surface low.

2) CYCLONE COLD-FRONT SIMULATION (6.67-km GRID)

The 8-h simulation was initialized 8 h into the 20-km simulation on a fine grid centered upon the cold front that is marked on Fig. 6a. The front is seen clearly in the sea level pressure field at 4 h (Fig. 8). Figure 8 represents the same time frame as Figs. 6a and 9a. In Fig. 8 a clear trough–ridge structure has developed at the front, which is now near the east boundary of the domain.

The vertical velocity about 1 km above the surface is shown in Fig. 9a and 9b at 4 and 6 h. Comparison of Fig. 9a with 7c reveals the significant extra detail as formerly elongated features along the cold front have been resolved into several distinct narrow lines of up-

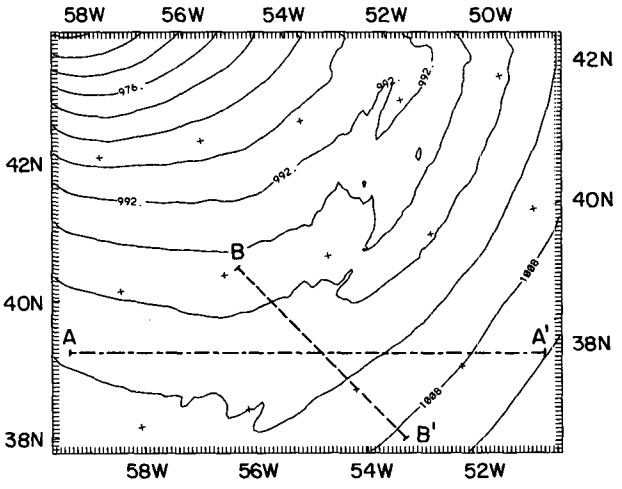

FIG. 8. The 6.67-km simulation, sea level pressure at 4 h. Contour interval is 4 mb. Area same as box in Fig. 6b.

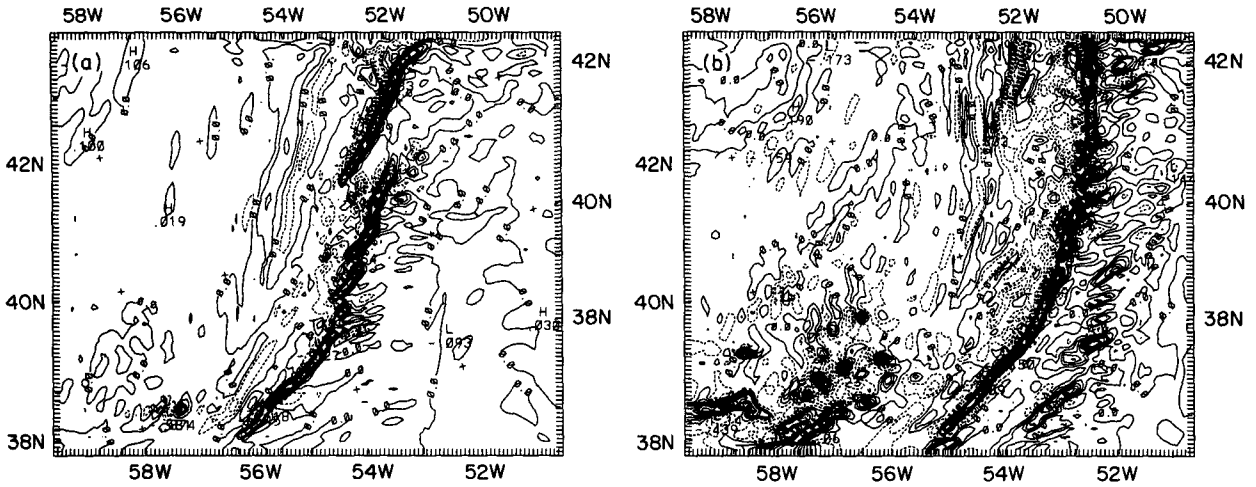

FIG. 9. The 6.67-km simulation, $\sigma = 0.865$, vertical velocity at (a) 4 h and (b) 6 h (negative dashed). Contour interval is 0.2 m s^{-1}.

ward motion with typical vertical motions of 1–2 m s^{-1}. Clearly defined "line elements" of varying lengths such as these are a well-documented feature of many observed cold fronts (James and Browning 1979; Hobbs and Persson 1982). The time evolution shows that between 4 and 6 h there is a merger into a single more continuous line followed in the next 2 h by evidence of fragmentation and new development to the rear and also possibly ahead at the southern end. Also at the end of the 8 h is evidence of the beginning of postfrontal shower activity noted in the simulations above.

The cloud (Fig. 10a) and rain (Fig. 10b) patterns at about the same height at 6 h show that the lines of ascent coincide with the rear edge of a 150-km-wide cloud band, and furthermore that there are rain cells at the front of this band as well as the more linear rainfall zone at the rear edge. The cloud band's persistence indicates the presence of a sharply defined broad mesoscale ascent ahead of the surface front. After about five simulated hours, cells growing within this region start to reach 10-km altitude above the front edge of the cloud band, and they produce the prefrontal rain seen in Fig. 10b. This feature is similar to the upper cold front seen by Browning and Monk (1982) in many katafronts but is not as widely separated from the surface front.

A vertical west–east section through the front at the position marked in Fig. 8 shows the southerly wind component at 4 h (Fig. 11a). In particular, note the upper-level frontal jet (50 m s^{-1}) at around 300 mb and the low-level prefrontal jet (33 m s^{-1}) at 900 mb and 150 km ahead of the front, which itself is a shallow zone of strong horizontal shear. The flow relative to the front is parallel throughout the troposphere in the postfrontal region.

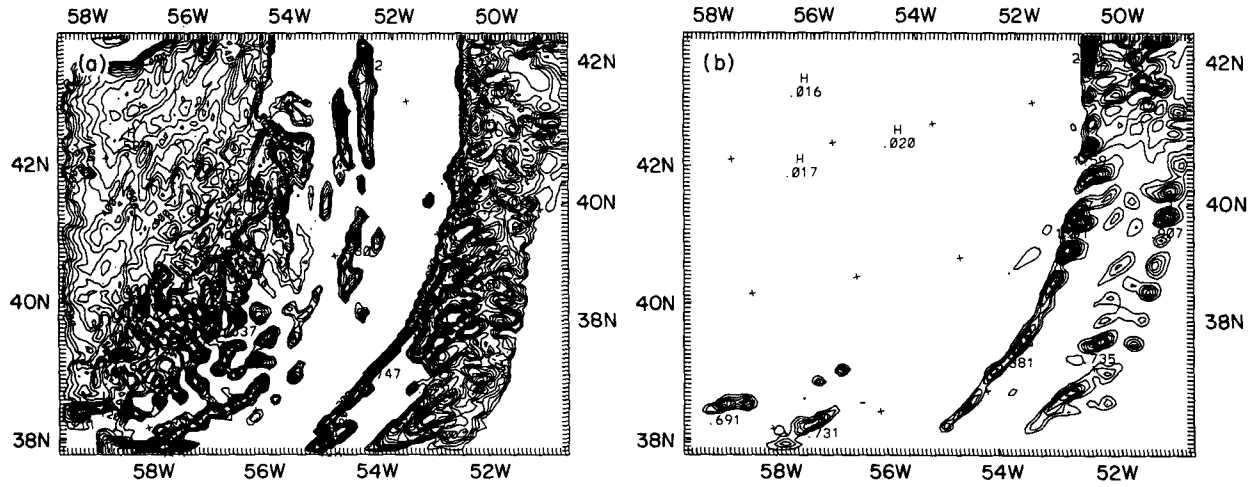

FIG. 10. The 6.67-km simulation, $\sigma = 0.865$, 6 h (a) cloud water, (b) rainwater. Contour interval is 0.1 g kg^{-1}.

c. *Cold-front dynamical aspects and sensitivity studies*

While only the larger-scale features of this cyclone were verifiable from observations, the cold-front simulation is of interest because it shows how fronts interact with a realistic large-scale flow in a model that includes physics representations of all the important processes that are likely to affect the dynamics. Here, a qualitative account of some of the frontal features is given. The complexity of the model and of the real atmosphere, however, make the understanding of the frontal structure difficult at a fundamental level unless modeling sensitivity studies are carried out to isolate causes and effects. The sensitivity studies described later will show how the removal of latent heating, surface fluxes, and friction separately affect the front. A hydrostatic simulation was also carried out on the 6.67-km grid and the results will show what gains are obtained with a nonhydrostatic model.

1) Dynamical aspects

The front at low levels is well defined by a narrow linear convergence zone with a corresponding updraft and strong vertical vorticity up to 10^{-3} s^{-1}. The similar broken nature of a northeastern Pacific cold front has been suggested by Hobbs and Persson (1982) to be a manifestation of cross-frontal shearing instability between the two air masses. This instability requires an inflection point in the front-parallel wind component. However, shearing instability alone would lead to waves with lengths of order five times the frontal width, that is, much shorter than the line elements seen in the simulation and generally seen in observations.

A complicating factor to the shearing instability mechanism is the strong convergence feeding the frontal updraft that would tend to stabilize the front to the growth of waves along it, and to advect instabilities aloft before they grow. In fact, enhanced eddy activity at higher altitudes is seen in the simulation, as discussed later in this section. For two dimensions Dritschel et al. (1991) have shown that a strain (deformation) of only one-quarter the magnitude of the shear is sufficient to suppress the growth of shearing instabilities. The convergence in the case of this front reaches twice the magnitude of the vertical vorticity but a three-dimensional theory is required to take into account both convergence and shearing.

Although the frontal temperature gradient is weak, there are localized cold pools barely resolved by the 6.67-km grid along parts of the cold front. These are produced by the evaporative cooling of rain from the linear updrafts as it falls into the low-humidity postfrontal air, particularly air from the 30–50-km-wide subsident slot immediately to the rear of the front. At the surface the narrow cold-frontal band may resemble a density current (Moncrieff 1989; Hobbs and Persson 1982). Local breaks in the front may therefore depend upon variability in the alongfront downdraft circulation, but it seems that the frontal eastward motion of 20 m s^{-1} is governed less by density current dynamics than by large-scale cyclone dynamics. We will return to this subject in the sensitivity studies described later.

The prefrontal jet of southerly wind (Fig. 11a) has a strong ageostrophic component as the isobars are oriented near southwest–northeast. The jet is likely due to a rightward Coriolis turning of the ageostrophic flow converging into the frontal updraft region, having an

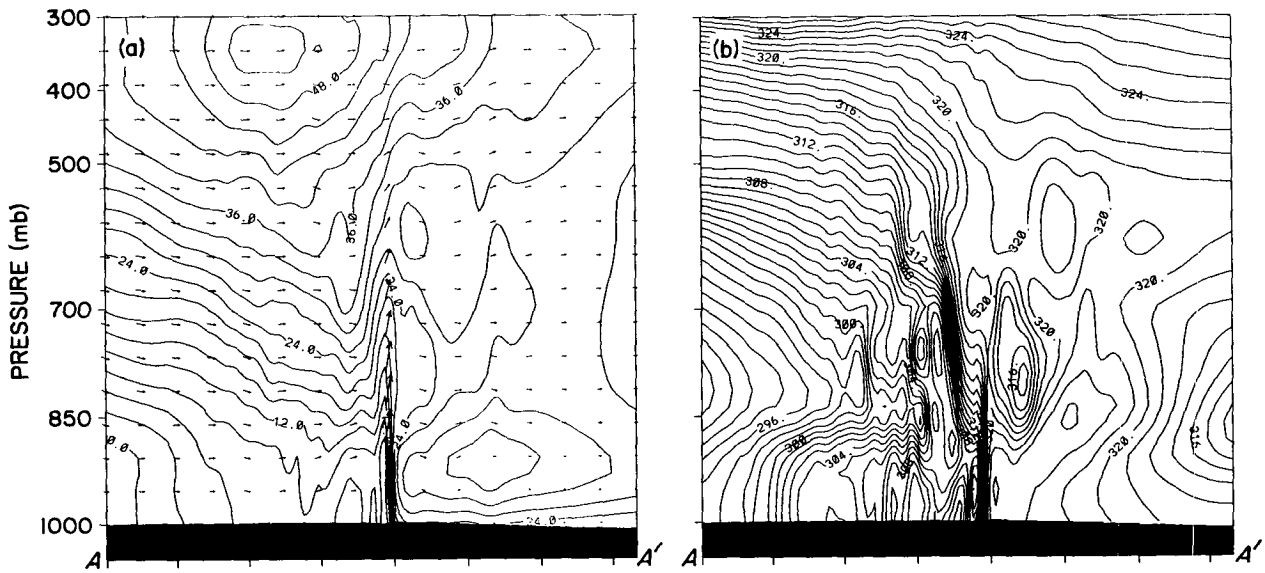

FIG. 11. The 6.67-km simulation, west–east vertical section at position AA' shown in Fig. 8, 4 h, (a) southerly wind component and arrows showing velocity in plane, (b) equivalent potential temperature. Linear pressure scale shown on left axis. Ticks at 100-km intervals. Contour intervals are 3 m s^{-1} and 1 K. Maximum vertical arrow is 158 μb s^{-1} and horizontal is 48 m s^{-1}.

elevated core due to surface friction. Note that the air within the jet is not moving parallel to the front or jet core but is approaching the front and will finally ascend in the frontal updraft.

The frontal updraft region itself is composed of the distinct linear cores as well as a less distinct band of ascending motion associated with the 150-km-wide cloud band (Fig. 10a), and at later stages a prefrontal line of convective cores develops in this band. Ascent within the cloud band at low levels is not uniform but comprises a series of southwest–northeast short bands of enhanced convective ascent detectable in Figs. 9a and 9b. A sensitivity study revealed that removing surface friction reorients these bands to be more perpendicular to the cold front. These results suggest that the short bands' orientation is related to the relative direction of low-level inflow to the frontal ascent region, which is sensitive to friction.

Soundings taken from the model and cross sections of θ_e (Fig. 11b) reveal that the 150-km broad frontal ascent column has a fairly homogeneous structure with a saturated, near moist-adiabatic lapse rate except for dry pockets around 700–900 mb that are apparently mixed horizontally from the postfrontal region. These dry pockets show as holes in the cloud band (Fig. 10a). Defined from these thermodynamic properties, the front itself is marked by an almost vertical boundary between the homogeneous moist ascending air and the stratified drier air, but the temperature field shows a classic rearward-sloped frontal interface with the upper jet consequently 100–150 km behind the surface front. This is a case where the definition of a front as an airmass boundary conflicts in position with its definition purely from the temperature field. The clear air ahead of the cloud band is capped by a weak stable layer probably resulting from compensating subsidence forced by the frontal ascent.

Thus, the picture that emerges is one of the well-documented broad warm conveyor belt in which conditionally unstable air saturates and ascends almost neutrally as it moves northward ahead of the surface cold front. However, embedded within this homogeneous conveyor belt are both cores of weak updrafts and pockets of postfrontal originating air. Prefrontal bands, and sometimes multiple bands, have frequently been observed with maritime cyclone cold fronts (e.g., Nozumi and Arakawa 1968; Harrold 1973; and Parsons and Hobbs 1983.)

There is an alongfront variation in updraft and cloud-top heights that systematically increase northward. The environment farther north along the front is modified by outflow advected from upstream updrafts and is thus moister and more favorable for downstream updrafts, these being less affected by entrainment of drier unmodified air.

The horizontal section of equivalent potential temperature at low to middle levels, particularly around 700 mb (Fig. 12), reveals a broad zone of resolved

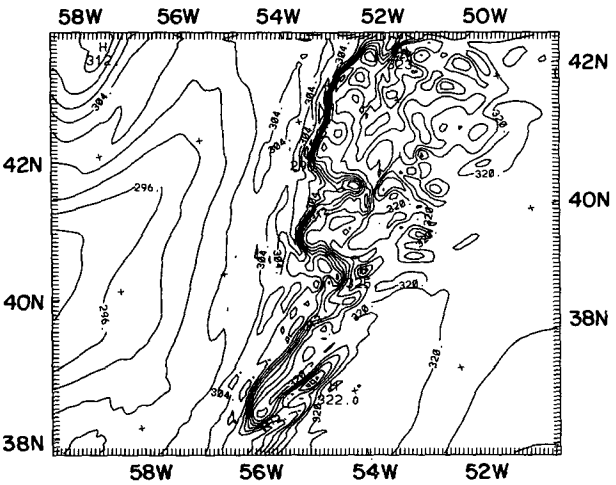

FIG. 12. The 6.67-km simulation, $\sigma = 0.65$, 4 h, equivalent potential temperature. Contour interval is 2 K.

eddies that seem to mix air across the frontal region. This is rather different from the sharp division of cold and warm air masses at lower levels. Harrold (1973) and others have documented an apparent overrunning of the surface front by midlevel drier air that may aid potential instability ahead of the front.

The cause of the eddy activity is not obvious, but it may be speculated that either inertial or shearing instability in the frontal zone is responsible. To support the former contention, the absolute momentum structure of the front should be examined, particularly the component parallel to the isobars. From Fig. 11a, which shows the southerly wind component, it can be seen that as air ascends in the frontal region it retains some low momentum from the surface convergence zone where the updraft originates. As the updraft reaches higher levels in the ambient alongfront shear, the low momentum within it becomes more anomalous compared to the ambient momentum. This leads to strong anticyclonic shear on the cold-air side of the updraft, and this is sufficient for negative absolute vorticity of magnitude $\zeta_a = -5f$; hence, the zone is inertially unstable. Expected growth time scales are of order $(\zeta_a f)^{-1/2}$ which is about 75 min.

Study of the absolute momentum parallel to the large-scale isobars, m, seen in Fig. 13, reveals that while this component is conserved in semigeostrophic motion, the value in the narrow frontal updrafts (e.g., the 44 m s^{-1} contour) is lower than in most of the warm surface-layer inflow with or without surface friction. In fact it is more comparable with m on the cold side of the surface front while its thermodynamic properties show no evidence of mixing across the front. It may be hypothesized that the updrafts' low absolute momentum originates from the reduction of m in the warm inflow by the front's *mesoscale* pressure pattern. The relative motion and orientation of the front to the

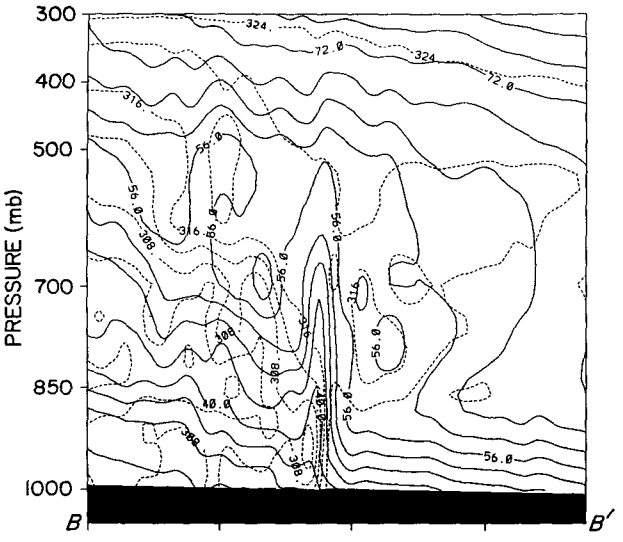

FIG. 13. The 6.67-km simulation, northwest–southeast cross section at position BB' in Fig. 8, of southwesterly absolute momentum m (solid) and equivalent potential temperature (dashed). Contour intervals are 4 m s^{-1} and 4 K. Ticks at 100-km intervals.

isobars (Fig. 8) allow the surface pressure gradient that is associated with the cold-air boundary to act as a source/sink for m. Through this pressure gradient, low m from the cold-air side of the front may be imparted to the updrafts.

Holt and Thorpe (1991) have observed the occurrence of "buckled m surfaces" at similar altitudes and of similar horizontal scales, 100 km, in a detailed study of east Atlantic cold fronts and have investigated the release of inertial instability in a two-dimensional idealized model. This instability would manifest itself as a preferential detrainment of updraft air toward the cold side of the baroclinic zone. Detailed cross-sectional soundings of a northeast Atlantic frontal zone show that a zone of well-mixed m on scales of only a few tens of kilometers exists on the cold-air side of the surface front at around 2–4 km in altitude.

Farther north, along the front where the frontal updrafts retain their low momentum to higher levels, a region of strong inertial instability develops on the warm (anticyclonic) side of the upper jet core at 250 mb. This region is characterized by eddies, probably inertial in origin, in contrast to the smooth flow in the rest of the domain at the same height. This instability, however, may not account for the enhanced dry-air eddies penetrating horizontally into the low-level warm cloud band, because the inertial instability is confined to the west of the front.

The mechanism of shearing instability is more likely to be responsible for the prefrontal eddies at 2–4-km altitude. The elevation of the eddies above the layer of strongest shear may be due to the mean vertical motion in the horizontally sheared zone, which transports instabilities upward as they grow. As seen in Fig. 11a, the shear is markedly reduced above 900 mb where the dry eddies exist (Fig. 11b), and the 100-km horizontal scale of the eddies (Fig. 12) is reasonably consistent with the 20-km width of the low-level sheared zone. Time scales of order 10^3 s would be associated with the lifting of this air to the altitudes of the eddies. Given that the vorticity reaches 10^{-3} s^{-1} this may be sufficient time for shearing instability to act. The lower-level smooth frontal structure is explained by the fact that as the air initially converges into the sheared frontal zone, it has not yet had time to develop finite-amplitude eddies.

2) SENSITIVITY STUDIES

Simulations were run that were identical to the above 6.67-km control case but with, respectively, no friction, no surface fluxes, and no latent heating. Additionally, one-way nesting from the hydrostatic 20-km simulation was used to provide a hydrostatic 6.67-km simulation with the same physics as in the nonhydrostatic control.

It was found that neither the removal of friction nor surface fluxes had a major impact on the front's motion or scales of ascent. Both tests produced narrow frontal updrafts, a prefrontal band development, and approximately a 1 m s^{-1} mean increase in frontal propagation over the first 6 h.

The observed differences were as expected for the no-friction case where surface winds were stronger leading in particular to the prefrontal jet extending to the surface and more vigorous postfrontal convection, probably as a result of the enhanced fluxes caused by stronger winds. The ascent in the frontal line elements was also typically increased by 30% as the removal of friction allowed greater convergence.

For the no-flux case there was a strong concentration of the surface temperature gradient at the front due both to the cooling of the frontal downdrafts and to cold advection being unopposed by heating from the warm ocean. The lowest few kilometers in the cold air mass were uniformly 2 K cooler by 6 h with no fluxes, and postfrontal shallow convection was absent even at 8 h when the other simulations began to show precipitation cores. The upper jet was unaffected by these differences; it was sensitive only to the large-scale tropospheric temperature gradients. The prevention of frontal collapse by surface heating has been documented in past studies of cyclones over warm oceans (e.g., Nuss and Anthes 1987; Kuo et al. 1991b).

The greatest impact upon frontal structure came from the removal of latent heating. Condensation and evaporation were still allowed but had no thermal effects. After 6 h the front was 150 km west of the control's position, having moved 14 m s^{-1} as compared to 20 m s^{-1}. The possible importance of evaporative cooling in driving the frontal motion, by forming a density current similar to squall-line downdraft outflows, was investigated with a simulation in which rain

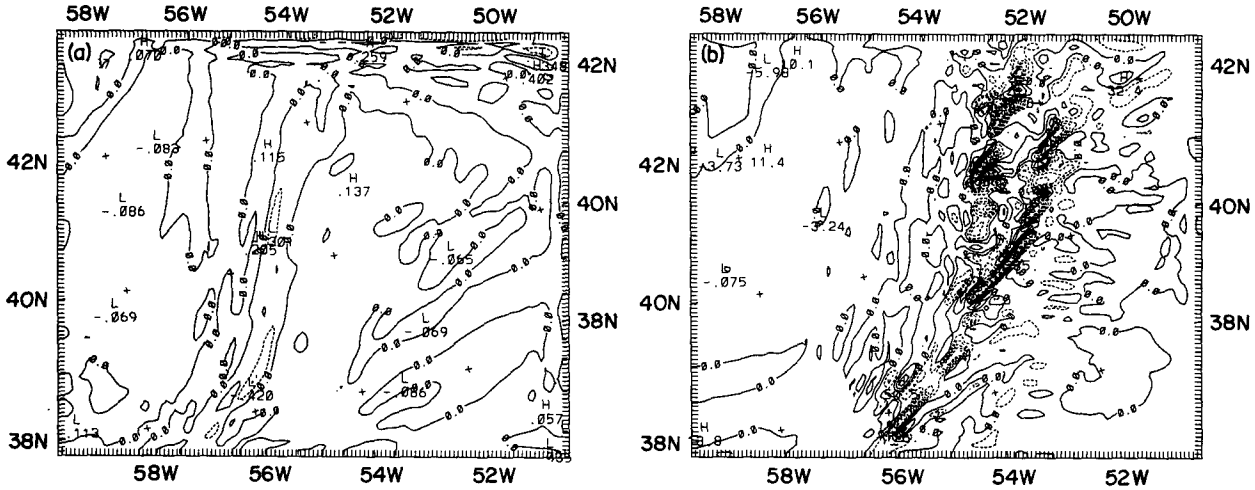

FIG. 14. The 6.67-km sensitivity simulations, $\sigma = 0.865$, 4 h, (a) vertical velocity with no latent heat, (b) $-\omega$ in hydrostatic simulation. Contour intervals are 0.2 m s^{-1} and 20 μb s^{-1}.

evaporative cooling was removed. This, however, demonstrated little difference from the control, showing that the speed difference of the front is governed by other dynamical factors associated with latent heating. Qualitatively, it seems plausible that the decreased effective static stability of prefrontal air with latent heating would allow the cold air to advance faster than in the case where latent heating is turned off and the warm air is much more stably stratified.

Another noticeable difference without latent heat was the lack of a frontal ascent and rainband; these elements were replaced by larger-scale ascent and rainfall across the warm sector as seen by comparing the vertical motion in Fig. 14a with Fig. 9a. The total rainfall without latent heat was only 7% less, so the overall ascent was comparable, but it was clearly deeper and more localized with latent heat.

Study of the geostrophic balance of the simulations at low levels reveals two areas of strongly ageostrophic motion seen in Fig. 15b, where it is calculated from a smoothed 950-mb height field. The first is accounted for by the subgeostrophic gradient wind effect as the flow curves strongly around the cyclone center situated just outside the northwest of the domain (Figs. 8 and 15a). The second ageostrophic region seen in Fig. 15b is a broad zone of 20–30 m s^{-1} easterlies toward the front in the warm sector, associated with convergence when latent heating is present. Little ageostrophic motion exists to the rear of the front, consistent with the frontal ascending branch being fed entirely by warm-

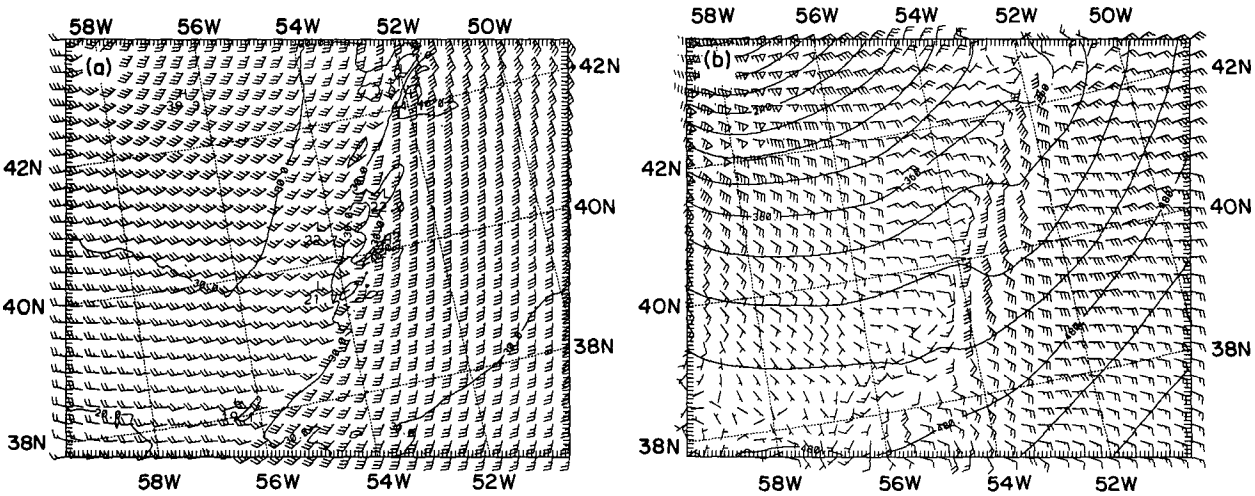

FIG. 15. The 6.67-km simulation, 950 mb, (a) wind barbs with wind speed contours, (b) ageostrophic wind component with smoothed geopotential height contours. Barbs in meters per second, contour intervals are 10 m s^{-1} and 30 m.

sector air. This ageostrophic convergence was absent in only the no-latent-heat simulation. This implies that the concentrated frontal ascent zone is due to an ageostrophic circulation set up by latent heat release in the control case. The reduced stability to saturated motion favors a smaller scale for the ascending branch than the stable dry descending branch of the frontal circulation (e.g., Eliassen 1959; Thorpe and Nash 1984).

Ascent exists in the warm sector as part of the baroclinic large-scale circulation. The role of latent heat is to concentrate this existing ascent onto a finer scale. Meanwhile friction resists the ageostrophic circulation leading to less convergence at the front than in a frictionless case. In other situations where friction dominates and convective effects are weaker, frictional convergence can act to concentrate the frontal updraft (Keyser and Anthes 1982), in contrast to the effect found here.

A hydrostatic simulation with the same physics on a 6.67-km grid showed results in general agreement with the nonhydrostatic model, indicating that hydrostatic dynamics are adequate for the generation of the mesoscale structures found. In particular, the line elements and prefrontal band still develop with similar vertical motion strengths and rainfall rates. This similarity is probably because vertical motions are not strongly buoyant. At 4 h into the simulations the hydrostatic line elements are shorter and less well defined, as shown by Fig. 14b compared to Fig. 9a, but by 6 h they are much like in the nonhydrostatic solution, indicating a possible lag in fine-structural development.

6. Conclusions

In this paper an adaptation of an existing hydrostatic model to give it a fully compressible nonhydrostatic capability has been described. This adaptation required the addition of a semi-implicit sound-wave solving routine to replace the pressure–momentum calculations, and prognostic equations for vertical momentum and pressure perturbation. Consideration was given to the use of temperature as a variable with perturbation pressure where consistency is required in the numerical treatment to preserve potential temperature. Also, the presence of a rigid upper boundary in this heightlike coordinate makes neglecting the small heating term in the pressure prediction equation preferable when trying to model diabatic processes in the real unbounded atmosphere.

The new model incorporates the initialization and physics routines that have been developed for the hydrostatic model specifically for the purpose of running real-data simulations and real-time forecasts. The extension to a nonhydrostatic basis will allow the model to maintain physical consistency on the higher-resolution grids that are now becoming possible with newer computers. Techniques of successive one-way nesting, such as the one demonstrated here, allow most synoptic-scale effects to be fed down to cloud scales. Fine-scale meteorological phenomena can now be simulated as they occur in situ with realistic and changing environmental conditions rather than in idealized, possibly unnatural environments.

In this paper, a particular example of an explosive cyclone simulation has been presented. The capability of the nonhydrostatic model to reproduce the hydrostatic model results at large scales was demonstrated. Using the larger-scale model to supply boundary conditions, simulations of the occlusion zone and cold-frontal region were carried out, providing a wealth of added detail. The fine structures associated with the cold front revealed by only a threefold decrease in grid length were particularly interesting for their similarity to observed features.

The frontal zone was well mixed in θ_e and nearly all saturated, so the ascent occurred in an upright band in near-neutral moist conditions. Convective cores embedded in this region formed a prefrontal band later in the simulation.

Both inertial and shearing instability appear to be important in explaining frontal features, and speculations were presented on their roles. The inertial instability results from air of low angular momentum being transported vertically by frontal ascent creating negative absolute vorticity at middle and high levels, and this results in lateral motion and mixing. The shearing instability results from a concentration of vorticity by low-level frontal convergence, but it only manifests itself as eddy motions a few kilometers above the front, probably due to vertical advection of the growing modes.

Sensitivity studies revealed how latent heating concentrates otherwise broad-scale ascent into a frontal band, generating a strongly ageostrophic flow converging on the front from the warm sector that is reduced slightly by surface friction. The frontal motion is also significantly reduced without latent heat.

For this case nonhydrostatic effects were not significant even on a 6.67-km grid, but it seems likely that cases with more buoyant convection would show more divergence from the hydrostatic solution on this grid scale. The model will continue to be developed with improvements in the physics, the introduction of two-way grid nesting and the addition of a four-dimensional data assimilation capability.

Further applications for the model include higher-resolution mesoscale simulations that can be used with dense observational networks and four-dimensional data assimilation to recreate the details of a mesoscale meteorological field. This information would be useful for cloud and radiative parameterization in global climate and forecast models. Even without additional observational data, comparisons can be made to determine how the mean properties of convective parameterization schemes in coarser-grid mesoscale models compare with those of resolved convection in fine-grid simulations.

Acknowledgments. I would like to thank Tom Warner and Bill Kuo for their support of this model development work, and the reviewers for their suggestions on improving this paper.

The project was funded by National Science Foundation Grants ATM-8711014 and ATM-9024434, Office of Naval Research Grant SFRC No. N00014-86-K-0688, NASA Grant NAGW 2686, and Department of Energy Grants DEFG02-90ER61071 and DEA105-90ER61070. The computing was carried out on NCAR's CRAY-YMP supported by the National Science Foundation.

APPENDIX

Finite-Difference Equations

The B-grid staggering of horizontal velocity variables with respect to the other fields was shown in Fig. 1. Vertical velocity is staggered vertically. Noting that the j index increments in the x direction, and i in the y direction, the conventional notation will be as follows:

$$\bar{a}^x = \frac{1}{2}(a_{i,j+1/2} + a_{i,j-1/2}), \tag{A1}$$

$$a_x = \frac{a_{i,j+1/2} - a_{i,j-1/2}}{\Delta x}. \tag{A2}$$

Multiple averaging terms such as $\bar{a}^{xyy}$ can also be defined as successive averages where the order of superscripts does not matter, for example,

$$\bar{a}^{xyy} = \overline{\bar{a}^x}^y.$$

Averaging vertically allows for nonuniform grid lengths and nonlinearly varying fields, such as temperature and water vapor by suitably weighting the values. The map scale factor $m(x, y)$ is included in these equations.

The spatial differencing of the terms in the horizontal momentum prediction equations is

$$\frac{\partial p_d^* u}{\partial t} = -m^2\left[\left(\bar{u}^x \frac{\overline{p_d^* u}^{xyy}}{m}\right)_x + \left(\bar{v}^y \frac{\overline{p_d^* v}^{xyx}}{m}\right)_y\right] - (\overline{p_d^* u}^{\sigma}\bar{\dot{\sigma}}^{xy})_\sigma + u\overline{\mathrm{DIV}}^{xy} - \frac{mp_d^*}{\bar{\rho}^{xy}}\left[\overline{p'_x}^y - \overline{(\sigma p^*)_x}^y \frac{\overline{p'_\sigma}^{xy\sigma}}{p^*}\right] + p_d^* fv + D(p_d^* u), \tag{A3}$$

$$\frac{\partial p_d^* v}{\partial t} = -m^2\left[\left(\bar{v}^x \frac{\overline{p_d^* u}^{xyy}}{m}\right)_x + \left(\bar{v}^y \frac{\overline{p_d^* v}^{xyx}}{m}\right)_y\right] - (\overline{p_d^* v}^{\sigma}\bar{\dot{\sigma}}^{xy})_\sigma + v\overline{\mathrm{DIV}}^{xy} - \frac{mp_d^*}{\bar{\rho}^{xy}}\left[\overline{p'_y}^x - \overline{(\sigma p^*)_y}^x \frac{\overline{p'_\sigma}^{xy\sigma}}{p^*}\right] - p_d^* fu + D(p_d^* v), \tag{A4}$$

where $p_d^* = \overline{p^*}^{xy}$ and DIV, the mass divergence term, is given by

$$\mathrm{DIV} = m^2\left[\left(\frac{\overline{p_d^* u}^y}{m}\right)_x + \left(\frac{\overline{p_d^* v}^x}{m}\right)_y\right] + p^*\dot{\sigma}_\sigma. \tag{A5}$$

The triple averaging in the horizontal momentum advection terms follows that of the hydrostatic model as discussed by Anthes (1972). The subgrid-scale and diffusion operators are represented by $D(a)$. The coordinate vertical velocity $\dot{\sigma}$ is obtained from

$$\dot{\sigma} = -\frac{\overline{\rho_0}^\sigma g}{p^*} w - \frac{m\sigma}{p^*}\overline{p_x^*}^x \overline{u}^{xy\sigma} - \frac{m\sigma}{p^*}\overline{p_y^*}^y \overline{v}^{xy\sigma}, \tag{A6}$$

and the vertical momentum equation is

$$\frac{\partial p^* w}{\partial t} = -m^2\left[\left(\overline{w}^x \frac{\overline{p^* u}^{y\sigma}}{m}\right)_x + \left(\overline{w}^y \frac{\overline{p^* v}^{x\sigma}}{m}\right)_y\right] - (\overline{p^* w}^{\sigma}\bar{\dot{\sigma}}^{\sigma})_\sigma + w\overline{\mathrm{DIV}}^{\sigma} + p^* g\frac{\overline{\rho_0}^\sigma}{\rho}\left(\frac{1}{p^*}p'_\sigma - \frac{1}{\gamma}\frac{\overline{p'T_0}^\sigma}{p_0 T}\right) + p^* g\frac{\overline{\rho_0}^\sigma}{\rho}\left(\frac{\overline{T'_v}^\sigma}{T} - \frac{R}{c_p}\frac{\overline{p'T_0}^\sigma}{p_0 T}\right) - p^* g\overline{(q_c + q_r)}^\sigma + D(p^* w). \tag{A7}$$

The pressure tendency equation, neglecting diabatic terms, is given by

$$\frac{\partial p^* p'}{\partial t} = -m^2\left[\left(\overline{p'}^x \frac{\overline{p^* u}^y}{m}\right)_x + \left(\overline{p'}^y \frac{\overline{p^* v}^x}{m}\right)_y\right] - (\overline{p^* p'}^{\sigma}\dot{\sigma})_\sigma + p'\mathrm{DIV} + p^*\rho_0 g\overline{w}^\sigma - m^2 p^*\gamma p\left[\left(\frac{\overline{u}^y}{m}\right)_x - (\sigma\overline{p^*}^x)_x \frac{1}{mp^*}\overline{u_\sigma}^{xy\sigma} + \left(\frac{\overline{v}^x}{m}\right)_y - (\sigma\overline{p^*}^y)_y \frac{1}{mp^*}\overline{v_\sigma}^{xy\sigma} - \frac{\rho_0 g}{m^2 p^*} w_\sigma\right], \tag{A8}$$

and temperature tendency is differenced as

$$\frac{\partial p^*T}{\partial t} = -m^2\left[\left(\overline{T}^x \overline{\frac{p^*u}{m}}^y\right)_x + \left(\overline{T}^y \overline{\frac{p^*v}{m}}^x\right)_y\right] - (\overline{p^*T}^\sigma \dot{\sigma})_\sigma + T(\mathrm{DIV}) + \frac{1}{\rho c_p}\left[p^* \frac{Dp'}{Dt} - \rho_0 g \overline{p^*w}^\sigma - D(p^*p')\right] + p^*\frac{\dot{Q}}{c_p} + D(p^*T), \quad \text{(A9)}$$

where Dp'/Dt is differenced like the corresponding terms in (A8). Moisture variables have similar advection forms to those in (A8) and (A9) except when using the upstream option where $\bar{q}^x$ is replaced by the upstream value alone.

The temporal differencing consists of leapfrog and forward steps and a semi-implicit time-splitting scheme described earlier. On the short time steps only the terms u, v, w, and p' vary, while the coefficients and right-hand-side terms in (1)–(4) are constant. Coefficients p, ρ, and T on the left-hand sides of these equations are updated on long time steps.

REFERENCES

Anthes, R. A., 1972: The development of asymmetries in a three-dimensional numerical model of a tropical cyclone. *Mon. Wea. Rev.*, **100,** 461–476.

——, and T. T. Warner, 1978: Development of hydrodynamical models suitable for air pollution and other mesometeorological studies. *Mon. Wea. Rev.*, **106,** 1045–1078.

Arakawa, A., and W. H. Schubert, 1974: Interaction of a cumulus cloud ensemble with the large-scale environment. Part I. *J. Atmos. Sci.*, **31,** 674–701.

——, and V. R. Lamb, 1977: Computational design of the basic dynamical process of the UCLA general circulation model. *Methods in Computational Physics,* **17,** Academic Press, 173–265.

Benjamin, S. G., and T. N. Carlson, 1986: Some effects of surface heating and topography on the regional severe storm environment. Part I: Three-dimensional simulations. *Mon. Wea. Rev.*, **114,** 307–329.

Brown, H. A., and K. A. Campana, 1978: An economical time-differencing system for numerical weather prediction. *Mon. Wea. Rev.*, **106,** 1125–1136.

Browning, K. A., and G. A. Monk, 1982: A simple model for the synoptic analysis of cold fronts. *Quart. J. Roy. Meteor. Soc.*, **108,** 435–452.

Carpenter, K. M., 1979: An experimental forecast using a nonhydrostatic mesoscale model. *Quart. J. Roy. Meteor. Soc.*, **105,** 629–655.

Clark, T. L., 1977: A small-scale dynamic model using a terrain-following coordinate transformation. *J. Comput. Phys.*, **24,** 186–215.

Cotton, W. R., and G. J. Tripoli, 1978: Cumulus convection in shear flow—Three-dimensional experiments. *J. Atmos. Sci.*, **35,** 1503–1521.

Dritschel, D. G., P. H. Haynes, M. N. Juckes, and T. G. Shepherd, 1991: The stability of a two-dimensional vorticity filament under uniform strain. *J. Fluid Mech.*, **230,** 647–665.

Dudhia, J., 1989: Numerical study of convection observed during the Winter Monsoon Experiment using a mesoscale two-dimensional model. *J. Atmos. Sci.*, **46,** 3077–3107.

Durran, D. R., and J. B. Klemp, 1983: A compressible model for the simulation of moist mountain waves. *Mon. Wea. Rev.*, **111,** 2341–2361.

Eliassen, A., 1959: On the formation of fronts in the atmosphere. *The Atmosphere and Sea in Motion,* B. Bolin, Ed., Rockefeller Inst. Press, 277–287.

Frank, W. M., and C. Cohen, 1987: Simulation of tropical convective systems. Part I: A cumulus parameterization. *J. Atmos. Sci.*, **44,** 3787–3799.

Grell, G. A., 1993: Prognostic evaluation of assumptions used by cumulus parameterizations. *Mon. Wea. Rev.*, **121,** 764–787.

Haltiner, G. J., and R. T. Williams, 1980: *Numerical Prediction and Dynamic Meteorology.* John Wiley and Sons, 477 pp.

Harrold, T. W., 1973: Mechanisms influencing the distribution of precipitation within baroclinic disturbances. *Quart. J. Roy. Meteor. Soc.*, **99,** 232–251.

Hobbs, P. V., and P. O. G. Persson, 1982: The mesoscale and microscale structure and organization of clouds and precipitation in midlatitude cyclones. Part V: The substructure of narrow cold-frontal rainbands. *J. Atmos. Sci.*, **39,** 280–295.

Holt, M. W., and A. J. Thorpe, 1991: Localized forcing of slantwise motion at fronts. *Quart. J. Roy. Meteor. Soc.*, **117,** 943–964.

Hsie, E.-Y., R. A. Anthes, and D. Keyser, 1984: Numerical simulation of frontogenesis in a moist atmosphere. *J. Atmos. Sci.*, **41,** 2581–2594.

Ikawa, M., 1988: Comparison of some schemes for nonhydrostatic models with orography. *J. Meteor. Soc. Japan,* **66,** 753–776.

James, P. K., and K. A. Browning, 1979: Mesoscale structure of line convection at surface cold fronts. *Quart. J. Roy. Meteor. Soc.*, **105,** 371–382.

Keyser, D., and R. A. Anthes, 1982: The influence of planetary boundary layer physics on frontal structure in the Hoskins–Bretherton horizontal shear model. *J. Atmos. Sci.*, **39,** 1783–1802.

Klemp, J. B., and R. B. Wilhelmson, 1978: Simulations of three-dimensional convective storm dynamics. *J. Atmos. Sci.*, **35,** 1070–1096.

——, and D. R. Durran, 1983: An upper boundary condition permitting internal gravity wave radiation in numerical mesoscale models. *Mon. Wea. Rev.*, **111,** 430–444.

Kuo, Y.-H., and S. Low-Nam, 1990: Prediction of nine explosive cyclones over the western Atlantic Ocean with a regional model. *Mon. Wea. Rev.*, **118,** 3–25.

——, L. Cheng, and J.-W. Bao, 1988: Numerical simulation of the 1981 Sichuan flood. Part I: Evolution of a mesoscale southwest vortex. *Mon. Wea. Rev.*, **116,** 2481–2504.

——, R. J. Reed, and S. Low-Nam, 1991a: Thermal structure of a simulated marine cyclone. Preprints, *First Int. Winter Storm Symp.,* New Orleans, Amer. Meteor. Soc., 372–376.

——, ——, and ——, 1991b: Effects of surface energy fluxes during the early development and rapid intensification stages of seven explosive cyclones in the western Atlantic. *Mon. Wea. Rev.*, **119,** 457–476.

Laprise, R., 1992: The Euler equations of motion with hydrostatic pressure as an independent variable. *Mon. Wea. Rev.*, **120,** 197–207.

——, and W. R. Peltier, 1989: On the structural characteristics of steady finite-amplitude mountain waves over bell-shaped topography. *J. Atmos. Sci.*, **46,** 586–595.

Mesinger, F., Z. I. Janjic, S. Nickovic, D. Gavrilov, and D. G. Deaven, 1988: The step-mountain coordinate: Model description and performance for cases of Alpine lee cyclogenesis and for a case of Appalachian redevelopment. *Mon. Wea. Rev.*, **116,** 1493–1518.

Miles, J. W., and H. E. Huppert, 1969: Lee waves in a stratified flow. Part 4: Perturbation approximations. *J. Fluid Mech.*, **35,** 497–525.

Miller, M. J., and R. P. Pearce, 1974: A three-dimensional primitive equation model of cumulonimbus convection. *Quart. J. Roy. Meteor. Soc.*, **100,** 133–154.

——, and A. A. White, 1984: On the non-hydrostatic equations in pressure and sigma coordinates. *Quart. J. Roy. Meteor. Soc.*, **110,** 515–533.

Moncrieff, M. W., 1989: Analytical models of narrow cold-frontal rainbands and related phenomena. *J. Atmos. Sci.*, **46,** 150–162.

Nozumi, Y., and H. Arakawa, 1968: Pre-frontal rainbands in the warm sector of sub-tropical cyclones over the ocean. *J. Geophys. Res.*, **73,** 487–492.

Nuss, W. A., and R. A. Anthes, 1987: A numerical investigation of low-level processes in rapid cyclogenesis. *Mon. Wea. Rev.*, **115,** 2728–2743.

Parsons, D. B., and P. V. Hobbs, 1983: The mesoscale and microscale structure and organization of clouds and precipitation in mid-latitude cyclones. Part XI: Comparisons between observational and theoretical aspects of rainbands. *J. Atmos. Sci.*, **40,** 2377–2397.

Queney, P., 1948: The problem of air flow over mountains: A summary of theoretical studies. *Bull. Amer. Meteor. Soc.*, **29,** 16–26.

Stauffer, D. R., and N. L. Seaman, 1990: Use of four-dimensional data assimilation in a limited-area mesoscale model. Part I: Experiments with synoptic-scale data. *Mon. Wea. Rev.*, **118,** 1250–1277.

Tanguay, M., A. Robert, and R. Laprise, 1990: A semi-implicit semi-Lagrangian fully compressible regional forecast model. *Mon. Wea. Rev.*, **118,** 1970–1980.

Tapp, M. C., and P. W. White, 1976: A nonhydrostatic mesoscale model. *Quart. J. Roy. Meteor. Soc.*, **102,** 277–296.

Thorpe, A. J., and C. A. Nash, 1984: Convective and boundary-layer parameterizations in a diagnostic model of atmospheric fronts. *Quart. J. Roy. Meteor. Soc.*, **110,** 443–466.

Tripoli, G. J., and W. R. Cotton, 1982: The Colorado State University three-dimensional cloud/mesoscale model—1982. Part I: General theoretical framework and sensitivity experiments. *J. Rech. Atmos.*, **16,** 185–220.

Wilhelmson, R. B., and C.-S. Chen, 1982: A simulation of the development of successive cells along a cold outflow boundary. *J. Atmos. Sci.*, **39,** 1466–1483.

Xue, M., and A. J. Thorpe, 1991: A mesoscale numerical model using the nonhydrostatic pressure-based σ-coordinate equations: Model experiments with dry mountain flows. *Mon. Wea. Rev.*, **119,** 1168–1185.

Zhang, D.-L., and R. A. Anthes, 1982: A high-resolution model of the planetary boundary layer—Sensitivity tests and comparisons with SESAME-79 data. *J. Appl. Meteor.*, **21,** 1594–1609.

——, and J. M. Fritsch, 1986: Numerical simulations of the meso-β scale structure and evolution of the 1977 Johnstown flood. Part I: Model description and verification. *J. Atmos. Sci.*, **43,** 1913–1943.

——, H.-R. Chang, N. L. Seaman, T. T. Warner, and J. M. Fritsch, 1986: A two-way interactive nesting procedure with variable terrain resolution. *Mon. Wea. Rev.*, **114,** 1330–1339.